MICROCOPY RESOLUTION TEST CHART

NATIONAL BUREAU OF STANDARDS-1963-A

AP-E301673

②

# AD-A154 374

DNA-TR-84-131

# STUDY OF A NOVEL SHIELDING PRINCIPLE FOR PROTECTION AGAINST INTENSE GAMMA-RAY BEAMS

W.L. Dunn
F. O'Foghludha
Applied Research Associates, Inc.
4917 Professional Court
Raleigh, NC 27609

15 March 1984

Technical Report

APPROVED FOR PUBLIC RELEASE;
DISTRIBUTION UNLIMITED.

DTIC
ELECTE
JUN 3 1985
B

DTIC FILE COPY

Prepared for
  Director
  DEFENSE NUCLEAR AGENCY
  Washington, DC 20305

# REPORT DOCUMENTATION PAGE

| 1a. REPORT SECURITY CLASSIFICATION UNCLASSIFIED | | | 1b. RESTRICTIVE MARKINGS | | | |
|---|---|---|---|---|---|---|
| 2a. SECURITY CLASSIFICATION AUTHORITY | | | 3. DISTRIBUTION / AVAILABILITY OF REPORT Approved for public release; distribution unlimited. | | | |
| 2b. DECLASSIFICATION / DOWNGRADING SCHEDULE N/A since UNCLASSIFIED | | | | | | |
| 4. PERFORMING ORGANIZATION REPORT NUMBER(S) C578 | | | 5. MONITORING ORGANIZATION REPORT NUMBER(S) DNA-TR-84-131 | | | |
| 6a. NAME OF PERFORMING ORGANIZATION Applied Research Associates, Inc. | 6b. OFFICE SYMBOL (If applicable) S.E. Div. | | 7a. NAME OF MONITORING ORGANIZATION Director Defense Nuclear Agency | | | |
| 6c. ADDRESS (City, State, and ZIP Code) 4917 Professional Court Raleigh, NC 27609 | | | 7b. ADDRESS (City, State, and ZIP Code) Washington, DC 20305 | | | |
| 8a. NAME OF FUNDING / SPONSORING ORGANIZATION | 8b. OFFICE SYMBOL (If applicable) | | 9. PROCUREMENT INSTRUMENT IDENTIFICATION NUMBER DNA 001-83-C-0399 | | | |
| 8c. ADDRESS (City, State, and ZIP Code) | | | 10. SOURCE OF FUNDING NUMBERS | | | |
| | | | PROGRAM ELEMENT NO 62715H | PROJECT NO B99QMXW | TASK NO C | WORK UNIT ACCESSION NO. DH007341 |

11. TITLE (Include Security Classification)

STUDY OF A NOVEL SHIELDING PRINCIPLE FOR PROTECTION AGAINST INTENSE GAMMA-RAY BEAMS

12. PERSONAL AUTHOR(S) W.L. Dunn
F. O'Foghludha

| 13a. TYPE OF REPORT Technical | 13b. TIME COVERED FROM 83/9/15 TO 84/3/15 | 14. DATE OF REPORT (Year, Month, Day) 1984 March 15 | 15. PAGE COUNT 72 |
|---|---|---|---|

16. SUPLEMENTARY NOTATION
This work was sponsored by the Defense Nuclear Agency under RDT&E RMSS Code
B310083466 C990MXWA00001 H2590D.

| 17 | COSATI CODES | | 18. SUBJECT TERMS (Continue on reverse if necessary and identify by block number) |
|---|---|---|---|
| FIELD | GROUP | SUB-GROUP | Gamma-Ray Shielding   Layered Shields   Monte Carlo |
| 18 | 6 | | Gamma-Ray Beams   Dose   Shield Geometry |
| 20 | 8 | | Shield Configuration   Buildup Factor |

19. ABSTRACT (Continue on reverse if necessary and identify by block number)

The work reported here draws attention to the geometrical disposition of shield elements as an important means of enhancing shield efficiency in a situation where, at first sight, the preponderance of Compton scattering seems to preclude improvements by any method other than increasing the total mass. The principal effort in Phase I has been to demonstrate the practical utility of using good geometry, for which purpose it has been necessary to develop a mathematical description of what good geometry - hitherto a vague and qualitative concept - actually is. The advantage of layering the shield or of making other geometrical modifications relying on the same theme, such as introducing thickness gradients, has also been investigated for situations in which the theoretically ideal geometry cannot be achieved because of fabrication constraints.

The importance of this Phase I study is that it verifies the dramatic effect of shield configuration on target dose, indicating the potentiality of methods for shield design other than the conventional mass-increase approach, and thus illustrates the

| 20. DISTRIBUTION / AVAILABILITY OF ABSTRACT ☐ UNCLASSIFIED/UNLIMITED ☒ SAME AS RPT ☐ DTIC USERS | 21. ABSTRACT SECURITY CLASSIFICATION UNCLASSIFIED | |
|---|---|---|
| 22a. NAME OF RESPONSIBLE INDIVIDUAL Betty L. Fox | 22b. TELEPHONE (Include Area Code) 202-325-7042 | 22c. OFFICE SYMBOL DNA/STT1 |

DD FORM 1473, 84 MAR

83 APR edition may be used until exhausted
All other editions are obsolete

20 ABSTRACT (Continued)
need to include geometric optimization as an essential component in overall shield design.  In this respect, a variant of the Monte Carlo method, called Inverse Monte Carlo, may be useful in future studies.

# SUMMARY

The work reported here draws attention to the geometrical disposition of shield elements as an important means of enhancing shield efficiency in a situation where, at first sight, the preponderance of Compton scattering seems to preclude improvements by any method other than increasing the total mass. The principal effort in Phase I has been to demonstrate the practical utility of using good geometry, for which purpose it has been necessary to develop a mathematical description of what good geometry - hitherto a vague and qualitative concept - actually is. The advantage of layering the shield or of making other geometrical modifications relying on the same theme, such as introducing thickness gradients, has also been investigated for situations in which the theoretically ideal geometry cannot be achieved because of fabrication constraints.

The fact that dose buildup factors can be as high as 10 or even 100 indicates the tremendous contribution that scattered radiation can make to the overall dose on the far (safe) side of a gamma-ray shield. The layering principle seeks to reduce this contribution by configuring the shield in such a way as to allow increased leakage of the scattered photons from the shield. In the course of studying this principle, a powerful and versatile Monte Carlo formalism has been developed which is easily extended to allow investigation of other more complex shield configurations involving for instance density gradients, lenticular layer profiles and curved- or conic-shaped shield members.

The importance of this Phase I study is that it verifies the dramatic effect of shield configuration on target dose, indicating the potentiality of methods for shield design other than the conventional mass-increase approach, and thus illustrates the need to include geometric optimization as an essential component in overall shield design. In this respect, a variant of the Monte Carlo method, called Inverse Monte Carlo, may be useful in future studies.

1

## TABLE OF CONTENTS

## LIST OF ILLUSTRATIONS

## LIST OF TABLES

# I. INTRODUCTION

Reduction of shield mass is of the greatest importance in the shielding of both space and terrestrial vehicles - in the space situation in order to minimize lift-off weight and in the terrestrial case because of terrain-loading and motive-power constraints. Efforts to reduce the mass are severely complicated in the range of gamma-ray energies delivered by nuclear weapons by the fact that Compton scattering is the principal attenuation mechanism in that energy-range. In these circumstances the attenuation in a shield of given cross-sectional area is independent of the nature of the absorbing material (with the exception of hydrogen) and thus the total mass is the primary factor determining shield efficiency.

This preliminary study examines the possibility of using the properties of the Compton scattering process to improve shield performance for a given mass, or to reduce the mass required for a specified performance. The two results of a Compton collision are (1) partial energy loss ("degradation") and (2) deflection ("scattering") away from the precollision photon trajectory which, for first collisions, is the line-of-sight connecting the source and target. It is clear that for a sufficiently large distance d between the initial collision site and the shielded object ("target" in the sequel) an arbitrarily large radial displacement r from the line-of-sight can be achieved if the photon collides only once in traversing the shield (Fig. I-1). Indeed, substantially all of the scattered photons emerging from a shield can be made to miss the target provided the ratio d/R (where R is shield radius) is sufficiently large and/or the shield is thin enough so that multiple scattering does not affect the attenuation - if there is more than one collision, a scattered photon that would otherwise have missed the target may be deflected inwards towards the line-of-sight once again.

The Fig. I-1 situation is usually referred to as "good" geometry while the case of very thick shields and/or small d/R ratios (Fig. I-2), where the potential shielding ability of the absorber is reduced by multiple scattering, is called "poor" geometry [1]. In this Phase I study we have attempted (1) to quantitatively investigate the notion of "good" geometry, and (2) to test a

5
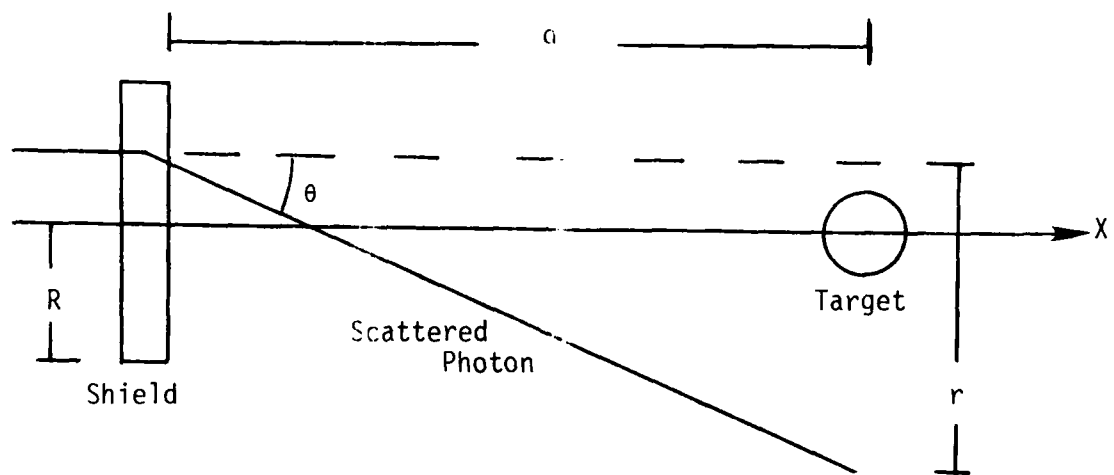
Figure I-1.  An Example of Good Geometry, with Large d/R
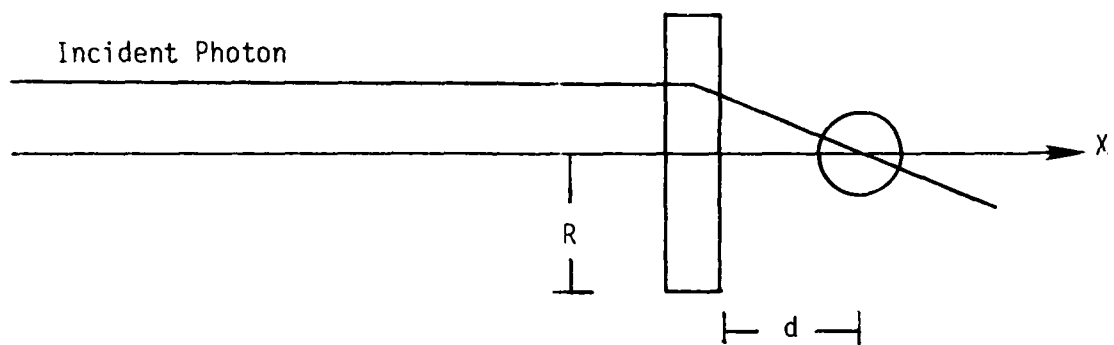


(a)  Small d/R
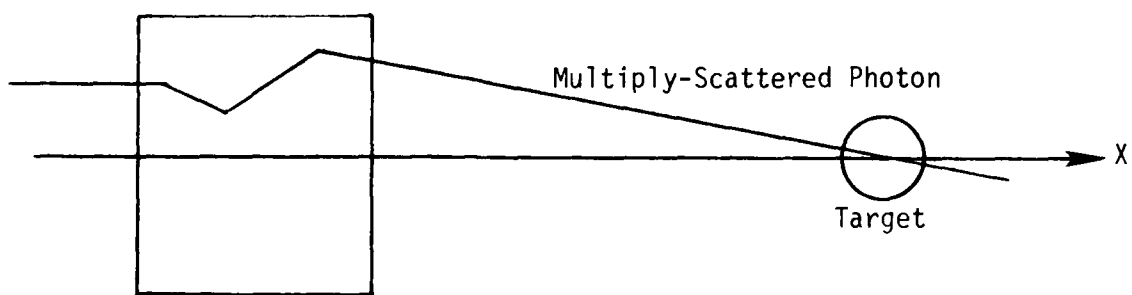


(b)  Thick Shield

Figure I-2.  Examples of Poor Geometry

novel modification of it in which splitting or layering of a shield mass may
improve performance by a repetitive use of good geometry. The application of
these and related concepts to practical situations is beyond the scope of this
investigation but will be addressed in a Phase II submittal.

A. Good Geometry

As far as the investigators are aware, no deliberate attempt to make use
of good geometry (much less of the modification of it we propose) to enhance
shielding has been made, although use of good geometries is sometimes forced
upon one in attempts to achieve some unrelated goal, e.g., to give consistent
results in certain absorption measurements [2] or as a means of improving film
contrast in radiographic magnification studies where the large d/R ratio is
used to reduce the effects of scattered radiation on the sensor [3]; there,
however, the total dose to the senior is essentially unaltered and the dose to
the target (i.e., the patient) is in fact increased.

The calculational method used in dealing with radiographic magnification
is semianalytic and of very limited power. The alternative Monte Carlo (MC)
method is much more versatile and powerful by virtue of its ability to treat
situations of almost arbitrary complexity. It has been applied, for example,
to the calculation of dose or fluence-related quantities at or immediately
contiguous to the exit face of plane-parallel slabs, such as in the determina-
tion of build-up factors [4], but does not seem to have been applied to the
calculation of dose quantities over the distant planes in which good geometry
is achieved. It was therefore proposed to develop the MC formalism in order
to study good-geometry conditions and the layering principle.

B. The Layering Principle

The premise of the layering proposal is that the exit face of a thick
shield is "fed" by a photon population comprised of (1) a relatively small
number of primary (undeflected) photons accompanied by (2) a much larger
number of scattered photons. Just as the arrival of the scattered exit flux
at the target can be considerably reduced by using good geometry, the "feed"
of multiple-scattered photons to the scattering layer immediately adjoining
the exit face can be reduced by ensuring that the last layer is in good
geometry with respect to the preceding layers, i.e., by layering the absorber

7

(Fig. I-3).  By introducing one or a series of similar layers, the feed from any one layer of the absorber to its successor can be reduced; thought of in another way, a layered geometry gives the photons scattering in a given layer an opportunity to "leak" laterally (and thus escape collision in deeper layers or in the target), while in an unlayered shield of the same total thickness lateral leakage is partially compensated for by scattering toward the line-of-sight.  The thrust of the Phase I proposal to investigate these matters was therefore to:

(1)  Develop the MC formalism, which involves the preparation of cross-section libraries, transport models for the specific geometry considered and techniques for scoring the desired quantities.  This permits the conditions for the existence of good geometry to be ascertained for any photon energy and any shield material.

(2)  Set up a code capable of dealing with arbitrary layer thicknesses and separations, shield materials and input spectra, and verify the operation of the code.

(3)  Use the code to test the improvement in the effectiveness of a given shield mass brought about by adjusting its configuration, i.e., to study the geometrical effects of shielding.

The initial code-implementation and application phase has been successfully completed and is described in this report.
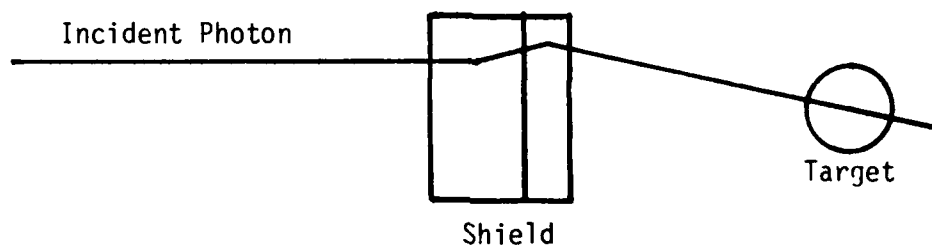
(a)  Contiguous Layers
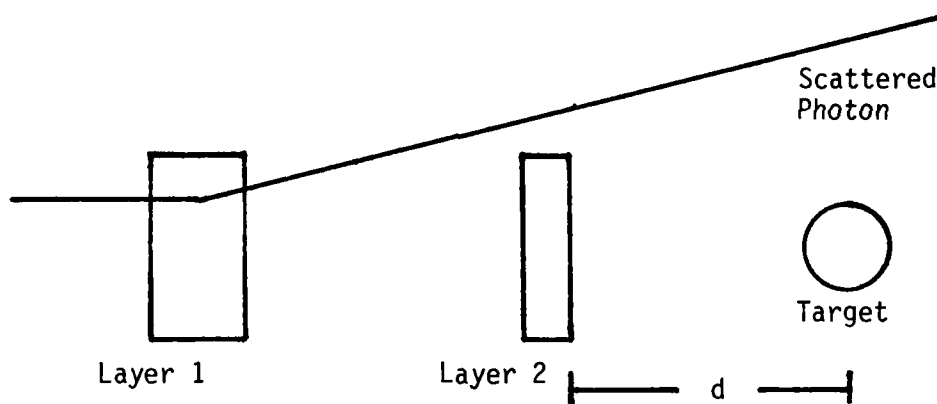
(b)  Separated Layers

Note:  A photon scattered in Layer 1 can be redirected toward the target if it enters Layer 2 (a), but "leaks" from the system when the layers are separated (b).

Figure I-3.  The Effects of Layering

## II. APPLICATION AND DESCRIPTION OF THE LAYERED SHIELD GEOMETRY

### A. Potential Applications

The concept of gamma-ray shield layering and configuration design has potential military applications for the obvious reasons that reduced shield mass directly reduces materials cost and in general improves the mobility of the shielded vehicle, but for other reasons as well. For instance, a layering also improves defense against projectiles from conventional weapons (it is well known that a single sheet of steel is more easily perforated than two separate sheets each of half thickness) and lends itself well to the construction of composite shields for protection against mixed gamma/neutron fields. Also, as will be shown under "Results", the shield geometry not only affects the total dose in the shielded volume but also the dose distribution. It thus may be possible to create local "cold spots" at regions occupied by personnel merely by proper configuration of the shield, not by increasing shield mass.

The subject of extension of the Phase I work will be treated in detail in a Phase II proposal; we wish here only to allude to the richness of this field of investigation. It has been shown in this work that the relative sizes and positions of uniform shield layers of constant thickness can significantly affect dose in the target; however, the use of more complex geometries, such as conic-section or curved-surface layers, may very well prove to have a greater effect. For instance, consider the situation portrayed in Fig. II-1a where the shield layer is a portion of a cone nappe. A photon interacting in the conic layer will generally have less material to penetrate, and thus greater chance for escape, than a similar photon in the plane-parallel layer of Fig. II-1b. Conic or other types of shaped layers thus appear to offer an enhanced potential for leakage from the shield after scatter. In addition, density and composition gradients may also offer advantages.

For the protection of ground-vehicles, we note that a series of thin curved layers as shown in Fig. II-2a might afford better protection than one thick shield (Fig. II-2b). A photon scattering in the outer layer can stream through the annular region between layers and either escape through the one

10
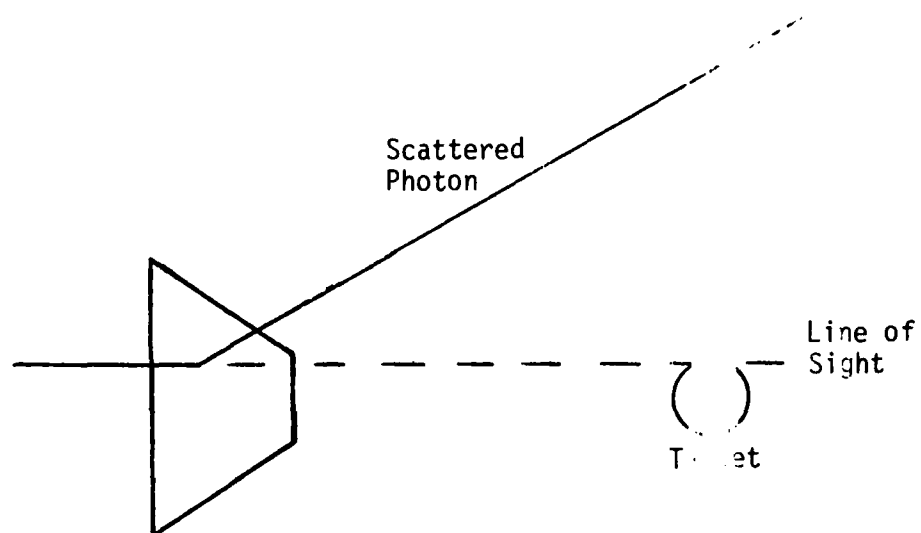
(a) Conic Section Shield Layer



(b) Plane-Parallel Shield Layer

Figure II-1.   Possible Advantages of Alternative
Shield Geometries

11
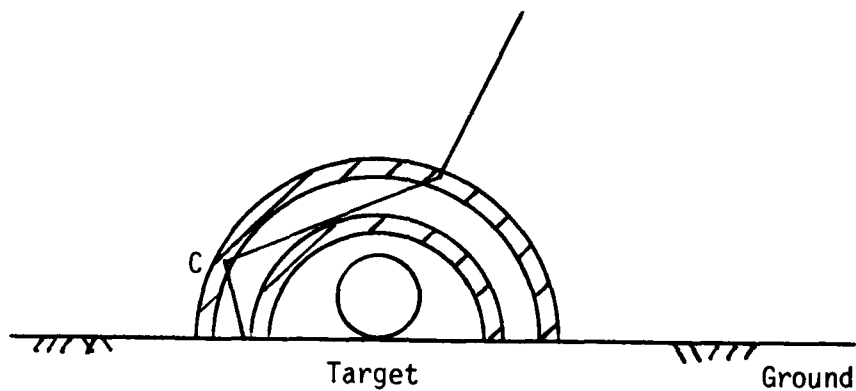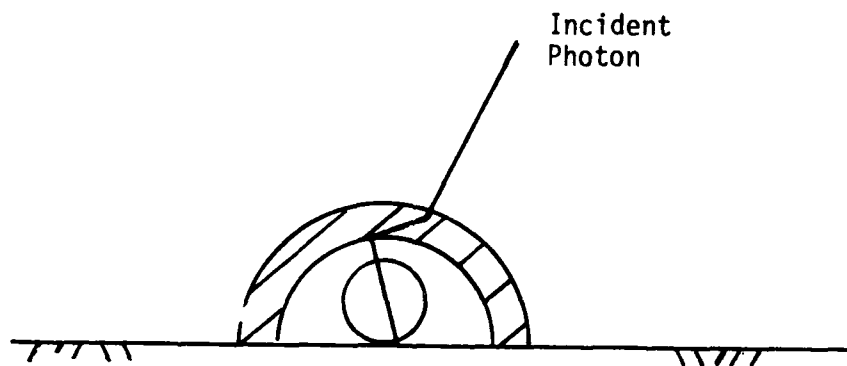
(a) Layered Shield

(b) Thick Shield

Figure II-2.  Potential Benefit from Streaming Between
Layers for Simplified Shielding Configuration in the Near-Ground Case

thin layer at C or scatter harmlessly down by virtue of its displacement to point C. More exotic designs are possible and may afford increased protection.

Finally we note that the fact that the MC method has been used to study the problem (and in fact is the traditional way of performing detailed dose calculations for armored vehicles) leads to the interesting possibility of applying the Inverse Monte Carlo (IMC) method [5] to the design optimization of the shields. This method, developed by the Principal Investigator, has been applied to radiative transfer inverse problems [6] and to the design of photon filters for radiation therapy [7]. It allows complex inve_e and optimization problems to be solved in a noniterative simulation and thus has potential application to efficient gamma-ray and neutron shield design.

## B. Geometry Conventions

The geometry we consider is quite simple. We assume a target volume is suspended in free space and subject to incident gamma radiation which originates at a distance P from the target. For finite P this leads to a slightly divergent gamma-ray beam; as P becomes infinite this reduces to a uniform, parallel beam. The assumption of a vacuous environment reduces the number of parameters and allows the feasibility of the layering principle to be studied in a more focused and isolated sense.

For generality and completeness, we consider the target to consist of either a right circular cylinder or a sphere and score the dose in each simultaneously, assuming the absence of the other. By considering a relatively large cylinder and a fairly small sphere, we can construct dose estimates typical of, say, a cockpit volume and a central-axis point. Both targets are assumed to be composed of water, which is approximately tissue-equivalent. The target cylinder has radius $R_c$ and length or thickness t; its central axis is colinear with the x-axis. The target sphere has radius $R_s$ and its center coincides with the center of the cylinder. The general target-shield geometry is shown in Fig. II-3a.

The shield is composed of $n \geq 0$ right circular cylindrical layers whose central axes are colinear with the x-axis and thus with the central axis of the target cylinder. The layers are all of the same radius, $R_\ell$, but have

13
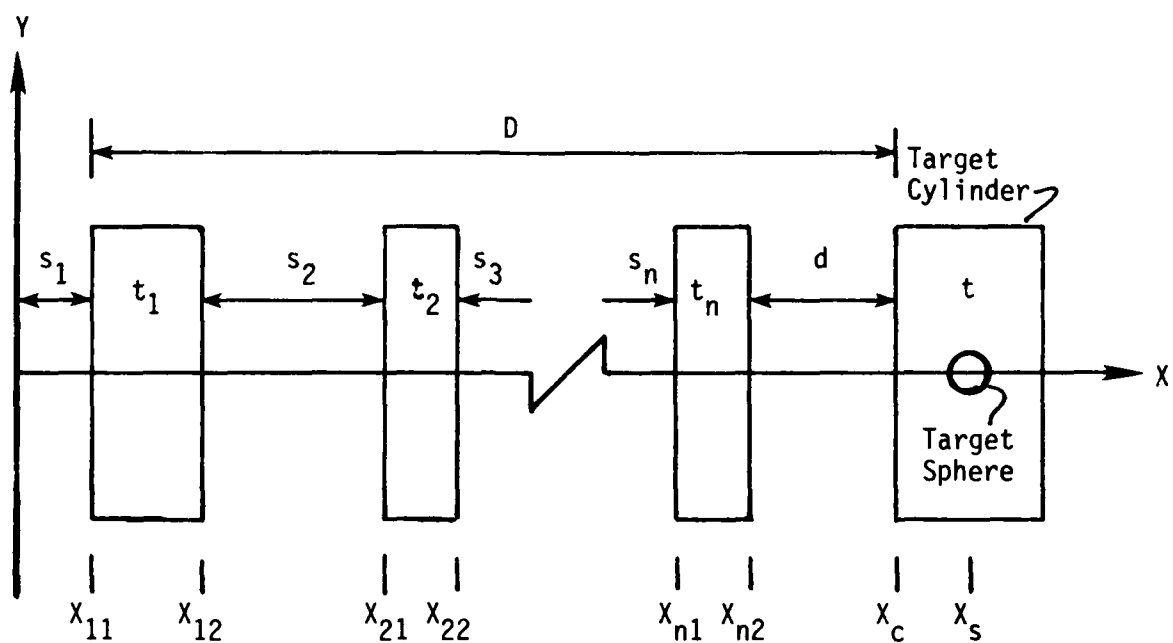
(a) General Case
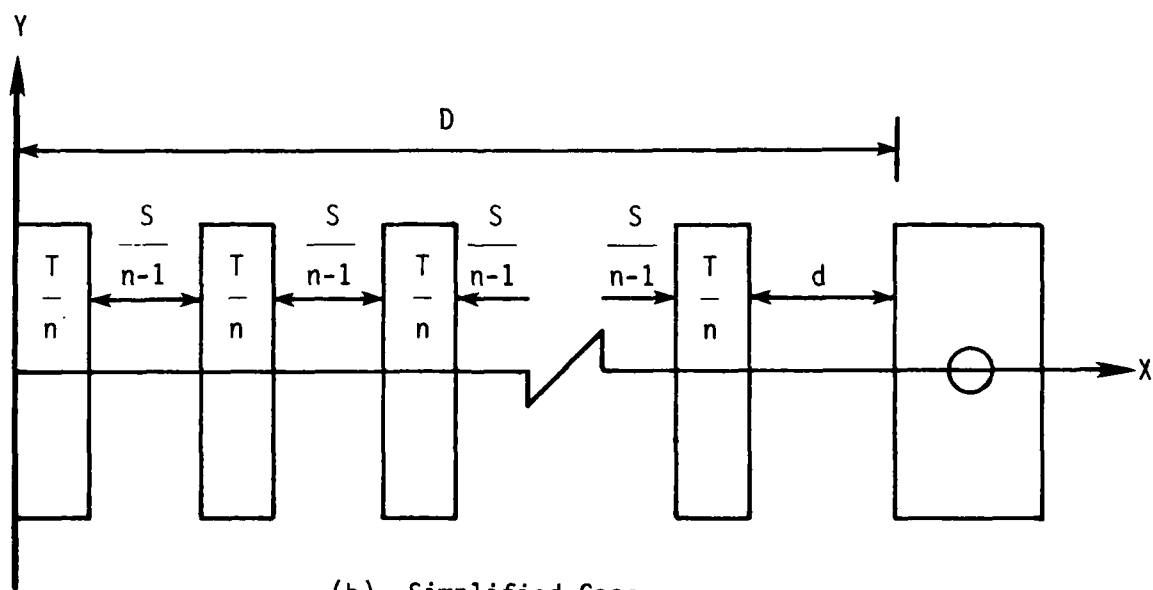


(b) Simplified Case

Figure II-3. Shield Layering Geometry

14

arbitrary thicknesses and separations. The thickness of the $i^{th}$ layer is denoted $t_i$ and the separation from the $i-1^{st}$ member is denoted $s_i$, as shown in Fig. II-3a. For this Phase I study, the shield layers consist of either lead (high Z, high density) or water (low Z, low density) and in a given case all layers must be of the same material and density.

We let d be the separation between the target cylinder and the nearest face of the closest layer, D the distance from the target cylinder to the front face of the first layer, T the total shield thickness, S the total spacing, $X_t$ the x-coordinate of the front face of the target cylinder and $(X_s,0,0)$ the coordinates of the center of the target sphere. We use the convention that $X_{i1}$ and $X_{i2}$ specify the x-coordinates of the front and back, respectively, of the $i^{th}$ shield layer. Then

$$T = \sum_{i=1}^{n} t_i \quad , \tag{1}$$

$$S = \sum_{i=1}^{n} s_i \quad , \tag{2}$$

$$D = X_t - s_1 = X_t - X_{11} \quad , \tag{3}$$

$$X_t = S + T + d \quad , \tag{4}$$

$$X_{i1} = \sum_{j=1}^{i} s_j - \sum_{j=1}^{i} j \tag{5}$$

and

$$X_{i2} = X_{i1} + t \quad . \tag{6}$$

We restrict ourselves to the case that $R_\ell = R_c$, i.e., the shield layers have the same radius as the target cylinder. This is done because a shield of smaller radius would allow direct irradiation of part of the target cylinder with no attenuation and a shield of larger radius would divert some photons toward the target that would otherwise stream by unaffected. In this general geometry, a given shield configuration is described by the number of layers, n, the target-to-shield distance, d, and the individual spacings, $s_i$, and thicknesses, $t_i$, for a total of 2n + 2 parameters.

In order to reduce the complexity of representing a shield configuration, we consider the simplified geometry of Fig. II-3b which is subject to the restrictions that the thicknesses are even,

$$t_i = T/n \quad , \quad i = 1,2,\ldots,n \quad , \tag{7}$$

and the spacings are even except for the first which is zero.

$$s_i = S/(n-1) \quad , \quad i = 2,3,\ldots,n \tag{8a}$$
$$= 0 \quad , \quad i = 1 \quad . \tag{8b}$$

Under these restrictions, we can represent a shield configuration by the four variables .., T, D and d. This geometry, depicted in Fig. II-3b, is referred to as the simplified geometry and will be used to represent most configurations discussed in the "Results" chapter.

It is noted that the azimuthal symmetry of the geometry considered would allow treatment of photon transport in a plane only. However, extension of this work to more complex geometries or to asymmetric incident gamma-ray distributions would require full 3-dimensional (3-D) transport simulation. Thus, the analysis and code development has used a 3-D transport model.

16

# III. THE MONTE CARLO MODEL

The direct Monte Carlo method provides a means of estimating expected values and hence definite integrals. The method is well established and has been used extensively in radiation transport calculations [e.g., 8-12]. Thus, the discussion here will concentrate on its application to the problem of interest rather than on the basis of the method itself. We do note, however, a few general points in order to establish our notation and conventions.

The Monte Carlo method is based on the Strong Law of Large Numbers, which basically states that the arithmetic average of a number of trials,

$$\hat{z} = \frac{1}{N} \sum_{i=1}^{N} z(\xi_i) \tag{1}$$

converges almost always to the true mean

$$\langle z \rangle = \int_a^b z(x) \, f(x) \, dx \tag{2}$$

in the limit of large N, i.e.,

$$\lim_{N \to \infty} \hat{z} = \langle z \rangle \quad , \tag{3}$$

where the $\xi_i$ are sampled from the probability density function (pdf), $f(x)$. Furthermore, the Central Limit Theorem provides a means to estimate the variance in the Monte Carlo estimator $\hat{z}$. Much of the power of the Monte Carlo method derives from the fact that variance reduction can be achieved by various means, such as biased sampling and contrived estimators. We will describe various variance-reduction procedures as they are applied to the layered shield problem, in particular the use of importance sampling, analytic equivalence and last-flight estimators.

The geometry we will consider was discussed in Chapter II and is shown in Fig. II-3. In the following sections we will consider photon transport through the shield layers and dose deposition in the targets.

## A.   Photon Transport

First, we specify the initial conditions.  These consist of the energy, $E$; direction, $\hat{\Omega} = (\alpha, \beta, \gamma)$ with $\alpha$, $\beta$, $\gamma$ the direction cosines; position, $(x,y,z)$; and statistical history weight, $W$.

### Initial Energy and Weight

The code allows two options for specifying initial energy:  mono-energetic ($n_e = 0$) and histogram ($n_e > 0$).  If $n_e = 0$, the source energy $E_0$ is input.  If $n_e > 0$, the spectrum cut-points, $E_j$, and cumulative fraction, $S_j$, are input (see Fig. III-1).  The energy is initialized to

$$E = E_0 \quad , n_e = 0 \tag{4a}$$

$$E = E_{j-1} + \xi(E_j - E_{j-1}) \quad , n_e \neq 0 \quad , \tag{4b}$$

where here and in what follows $\xi$ is a random variate sampled uniformly from the unit interval $(0,1)$.  The particular $j$ used in Eq. 4b is determined by the condition

$$S_{j-1} < \xi < S_j \quad , \tag{5}$$

where $S_0 = 0$ and $\xi$ is a separate uniform random variate.  The history weight is initialized to unity,

$$W = 1 \quad . \tag{6}$$

### Initial Position and Direction

The initial position is determined by sampling an $r$ and $\phi$ (see Fig. III-2a) so as to give a uniform distribution over the area of a circle, using

$$r = R_\ell(\xi_1)^{1/2} \tag{7a}$$

and

$$\phi = 2\pi\xi_2 \quad , \tag{7b}$$

and then letting

$$x = X_{11} \tag{8a}$$

$$y = r\,\sin\phi \tag{8b}$$

$$z = r\,\cos\phi \quad . \tag{8c}$$

18

Fractional Part of Spectrum



Cumulative Fraction
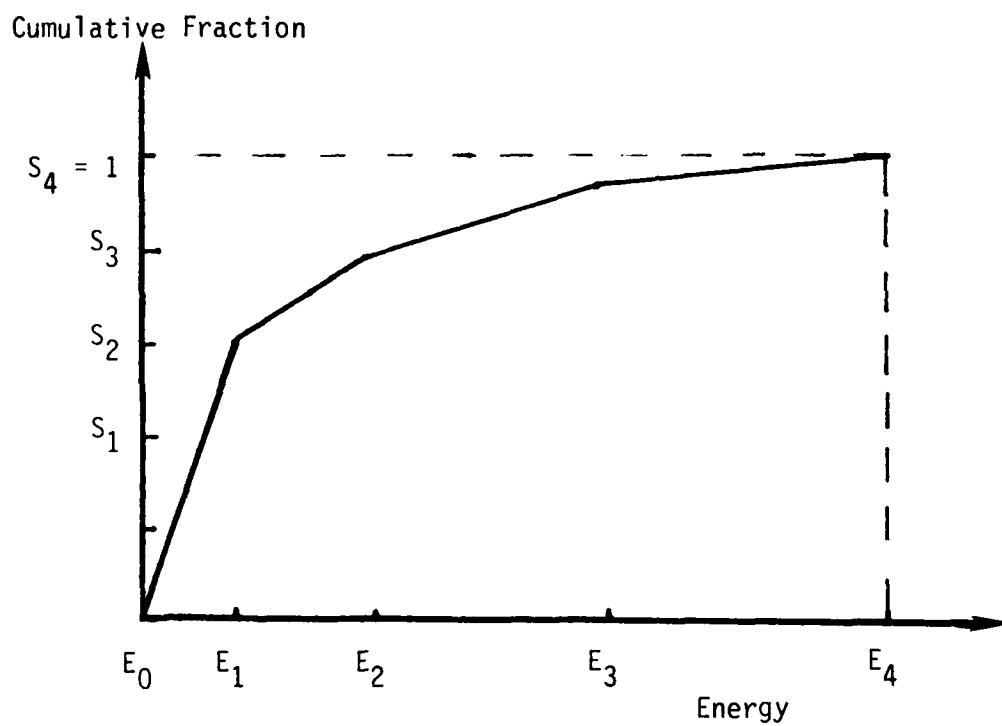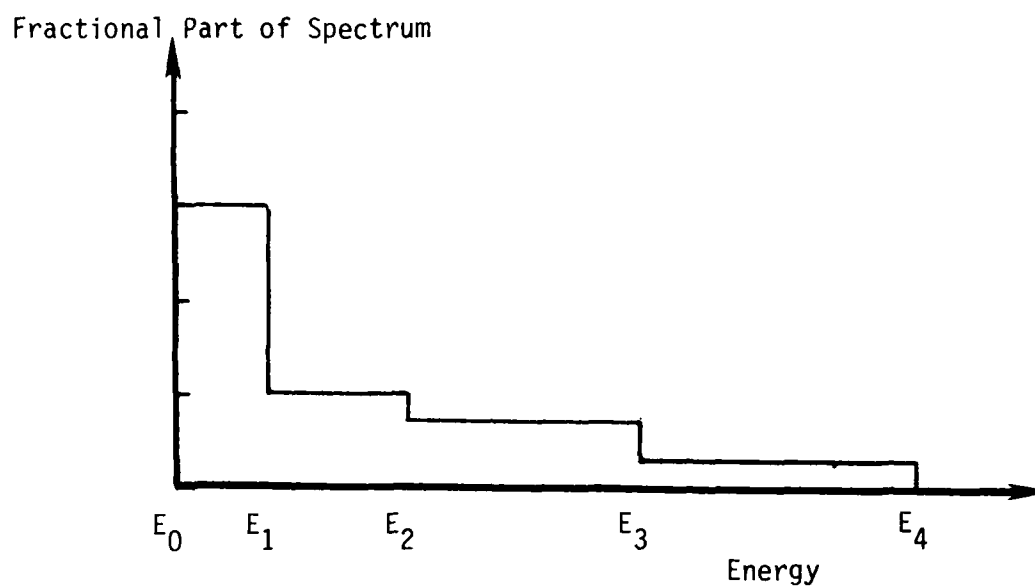


Figure III-1.  Example Photon Spectrum

19
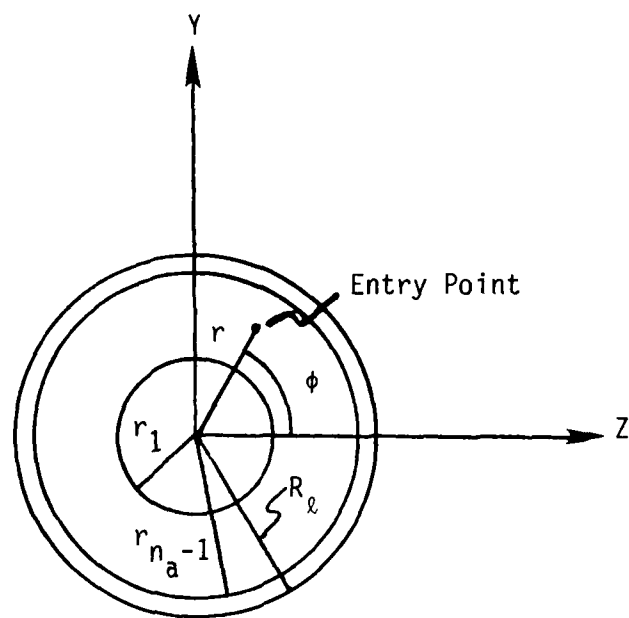
(a)  Front View, Showing First and Last
Annular Regions (of Equal Areas)
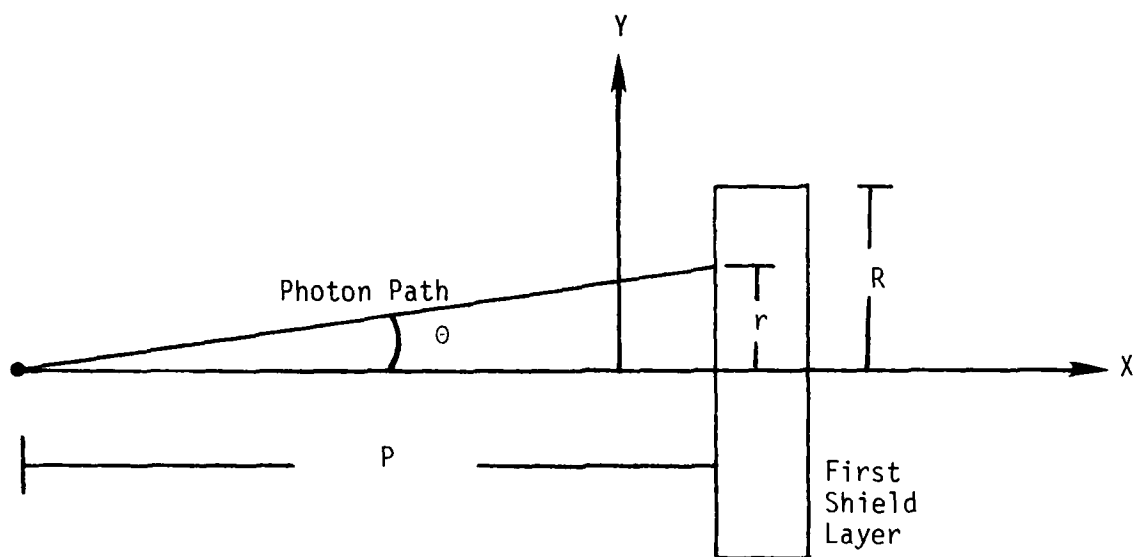


(b)  Side View, Showing Remote Source Point

Figure III-2.  Geometry of Photon Incident on First Layer

20

For later purposes, we wish to keep track of the radial position that the photon entered the first layer. To accomplish this, we construct annuli of equal area on the front face of the first layer, as in Fig. III-2a, and store the annulus number, I, corresponding to the entry point such that $r_{I-1} < r < r_I$, where $r_i$ is the outer radius of annulus i. These radii are determined by requiring that the area of each annulus be

$$A_0 = \frac{\pi R_\ell^2}{n_a} \quad , \tag{9}$$

where $n_a$ is the number of annuli. Then,

$$r_i = [r_1^2 + r_{i-1}^2]^{1/2} \quad , \quad i \geq 1 \quad , \tag{10}$$

with $r_0 = 0$.

The initial direction is determined by assuming the radiation originates at a point a stance P from the first shield layer (Fig. III-2b). Under these conditions, the initial direction cosines are given by

$$\alpha = \cos\theta \tag{11a}$$

$$\beta = \sin\theta \, \sin\phi \tag{11b}$$

$$\gamma = \sin\theta \, \cos\phi \tag{11c}$$

where

$$\theta = \tan^{-1} (r/P) \quad , \tag{12}$$

and r and $\phi$ are given by Eqs. 7. In the limit of infinite P, the beam is parallel and Eqs. 11 reduce to $\alpha = 1$, $\beta = \gamma = 0$; this is the normal case we have treated although Eqs. 11 were used in one study to consider a diverging beam.

### Determine Position and Type of Interaction

In order to determine how far the photon travels before interacting, we must determine the total linear attenuation coefficient, $\mu$, of the shield material. (In this Phase I study we have assumed that all shield layers consist of the same materials; however, the code has been written so that different compositions and densities can be input for the various layers so that in Phase II more elaborate shield configurations, for instance having

21

atomic number or density gradients, can be studied.) We will also need the various partial cross sections for Compton (incoherent) scattering, $\sigma$, photoelectric absorption, $\tau$, and pair production, $\kappa$, in order to determine the type of interaction. Thus, we call a subroutine that calculates, using piecewise polynomial approximation, the cross sections $\sigma$, $\tau$, $\kappa$ and their sum

$$\mu(E) = \sigma + \tau + \kappa \quad , \tag{13}$$

given the photon energy, E. We have not included Rayleigh (coherent) scattering nor bound electron effects on the Compton process in this Phase I study because these involve small-angle scattering and the Rayleigh cross section is generally small; hence these effects are not needed in order to establish feasibility. However, both effects would be included in the Phase II study since optimizing shield design using the layering principle would require proper treatment of even small-angle scatters.

The distance to interaction, s, is obtained by sampling from the pdf

$$f(s) = \mu \, e^{-\mu s} \quad , \tag{14}$$

from which we obtain

$$s = - \frac{\ln \xi}{\mu} \quad . \tag{15}$$

The coordinates of the photon are easily updated to the new interaction point using

$$x' = x + s\alpha \tag{16a}$$

$$y' = y + s\beta \tag{16b}$$

$$z' = z + s\gamma \quad . \tag{16c}$$

In applying Eqs. 16, we check to see that s is less than the distance, $\Delta$, to the nearest boundary (see Fig. III-3). If so, Eqs. 16 are used directly; if not, the photon has escaped the shield layer and we must perform the following procedure:

(1) If the photon exits through the cylindrical surface, the history is terminated (path 1 in Fig. III-3).

22
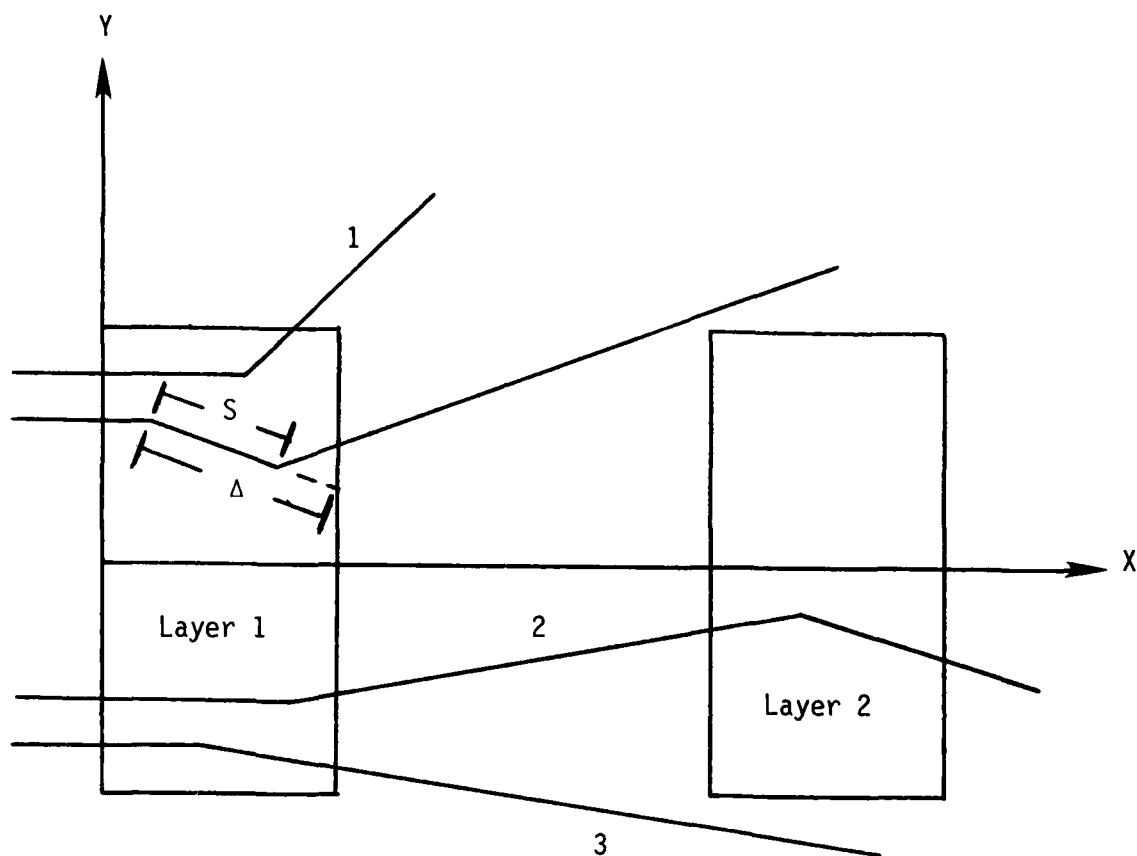
Figure III-3.  Possible Photon Paths in Layered
Shield Configuration

(2) If the photon escapes through a planar surface, we update the photon position to the exit point, reduce the distance s by the distance through this layer Δ, find the intersection with the next layer (if any), position the photon at this entrance point, apply Eqs. 16 with (x,y,z) representing the entrance point and s the path length reduced by the distance Δ, and repeat the process (path 2 in Fig. III-3). If there is no intersection with another layer, the history is terminated (path 3 in Fig. III-3).

The photon paths from incidence on the first shield layer to first interaction, from one interaction to another or from one interaction to entry into one of the targets are straight-line segments. To determine where a given path intersects shield or target boundaries, we must be able to find the intersection of a ray starting at $(x,y,z)$ and having direction $(\alpha,\beta,\gamma)$ with planar, cylindrical and spherical surfaces. We let the intersection point be $(x_c, y_c, z_c)$ and occur at radial distance $r_c$ from the x-axis. The determination of these intersection points is straightforward; for completeness the solutions are presented in Appendix A. The distance between $(x,y,z)$ and $(x_c, y_c, z_c)$ is then simply

$$\Delta = [(x_c - x)^2 + (y_c - y)^2 + (z_c - z)^2]^{1/2} \ . \tag{17}$$

## Force Scatter

Since the pair production interaction is inevitably followed by annihilation of the positron and emission of two 0.511 MeV gamma-rays, we treat it for shielding purposes as a scattering interaction. We refer to this "scatter" as pair production/annihilation (PP/A). This interaction leads to one 0.511 MeV photon emitted isotropically and a second 0.511 MeV photon antiparallel to the first. The other scattering interaction we treat is the incoherent scatter, referred to as Compton (C). We do not include the scatter-function correction for bound electron effects and we neglect coherent (Rayleigh) scattering. The final interaction we consider is the photoelectric effect (P), which is the complete transfer of the photon energy to a bound electron.

We force scatters as a variance reduction measure to improve the efficiency of the simulation. Since P interactions remove photons from consideration, they can no longer deposit energy in the target, the event we are

24

interested in scoring. Thus, we pick PP/A interactions with frequency $\kappa/(\tau + \kappa)$ and C scatters the rest of the time. This requires that we weight the history by the factor

$$W = \frac{\tau + \kappa}{\mu} \ , \tag{18}$$

which is the probability of scatter. All cross sections are of course determined at the current photon energy.

### Find Post-Scatter Conditions

If $\xi < \kappa/(\tau + \kappa)$, we treat the interaction as an isotropic scatter. Letting $\phi$ be azimuthal angle and

$$\omega = \cos \theta \tag{19}$$

where $\theta$ is the scatter angle, we sample to obtain

$$\omega = 1 - 2 \ \xi_1 \ , \tag{20a}$$

$$\phi = 2\pi \ \xi_2 \ , \tag{20b}$$

then update the direction cosines using the formulas of Selph and Garrett [11]

$$\alpha' = \alpha \ \omega + \frac{\sin \theta}{\Gamma} \ [\alpha \ \gamma \ \cos\phi - \beta \ \sin\phi] \tag{21a}$$

$$\beta' = \beta \ \omega + \frac{\sin \theta}{\Gamma} \ [\beta \ \gamma \ \cos\phi + \alpha \ \sin\phi] \tag{21b}$$

$$\gamma' = \gamma \ \omega - \Gamma \ \sin\theta \ \cos\phi \ , \tag{21c}$$

where

$$\Gamma = (1 - \gamma^2)^{1/2} \tag{22}$$

and $(\alpha',\beta',\gamma')$ are the direction cosines after the scatter. We save the negative values of these direction cosines and the values of W, x, y, and z for later simulation of the second photon resulting from the positron annihilation.

If $\xi > \kappa/(\tau + \kappa)$, we treat the interaction as a Compton scatter. We sample the azimuthal angle as in Eq. 20b and determine the cosine of the scatter angle in the following manner. We sample $\delta$ from the normalized version of $g(\delta|\eta)$ in Eq. B-9b (see Appendix B),

$$g_n(\delta|\eta) = \frac{g(\delta|\eta)}{D} , \qquad (23)$$

where D is given by Eq. B-14, and use Eq. B-5 to obtain $\omega$, i.e.,

$$\omega = \frac{\eta + 1 - \delta}{\eta} , \qquad (24)$$

where

$$\eta = \frac{E}{0.511} . \qquad (25)$$

The procedure used to sample from $g_n$ is a version of the Kahn [8] rejection technique taken from Dunn and Gardner [13]. We then update the direction cosines according to Eqs. 21 and determine the post-scatter photon energy from

$$E' = E/\delta . \qquad (26)$$

Whether a PP/N or C scatter was chosen, we test to see if the product of history weight and photon energy is larger than some input cutoff value, $\epsilon$. If not, we terminate the photon history since the additional contribution to the dose in the target would be negligible; if so, we continue the simulation by calculating the cross sections at the new energy and proceeding as discussed in the section "Determine Position and Type of Interaction."

B. Target Scoring

We score two target dose quantities, one typical of the central-axis, first-collision dose and one representative of the total dose deposited in a larger mass. The descriptors are actually fractional energy depositions, representing energy deposited in the target per unit energy incident on the shield front face. The central-axis descriptor is defined as the expected energy deposited in the target sphere by first collisions in the sphere per unit energy incident on the front shield face; it is denoted $F_s$ and is expressed in units of eV/MeV (eV deposited per MeV incident). By first-

26

collision we mean that any secondary photons born in the first collision within the sphere are assumed to escape the sphere. On the other hand, all energy given to electrons is assumed to remain in the sphere. The quantity scored for the larger cylindrical target is denoted $F_C$ and is defined as the total energy deposited in the cylinder (in keV), including that from secondary photons, per MeV incident on the first shield layer. Thus, for the target cylinder we track both primary and secondary photon transport through the cylinder.

We score the quantity $F_C$ using a last-flight estimator. Thus, for every photon path, including the incident one, we extend the path to see if it intersects the target cylinder. If so, we determine the total distance, $\delta$, through all shield layers along this path and allow the photon to enter the cylinder with weight $e^{-\mu\delta}$, where $\mu$ is the total linear attenuation coefficient of the shield material at the current photon energy. We then force an inter-action in the target with weight $1 - e^{-\mu_t\delta_t}$, where $\mu_t$ is the total linear attenuation coefficient of the target material at the current photon energy and $\delta_t$ is the distance through the target to escape.

At each interaction point in the target cylinder we score average energy deposited with the estimator $[\sigma_t\bar{T} + \tau_t E + \kappa_t(E-1.022)]/\mu_t$, where $\bar{T}$ is the average energy deposited in a Compton collision at the current photon energy, $E$, and the subscript t refers to the target cylinder. The determination of $\bar{T}$ is discussed in Appendix B. We then force a PP/A or C interaction, with weight $(\sigma_t + \kappa_t)/\mu_t$, sample to determine which of the two occurs and continue simulation through the target, scoring average energy deposition at each interaction point and terminating when the product of photon weight and energy is reduced below the cutoff, $\epsilon$. After termination, we return to the original interaction point in the shield and resume photon transport through the shield. Thus, the cylinder energy deposition estimator for a given history has the form

$$\Delta E_C = e^{-\mu\delta} \sum_{j=1}^{\nu} \left\{ \frac{(\sigma_t + \kappa_t)}{\mu_t} (1 - e^{-\mu_t\delta_t}) \frac{[\sigma_t\bar{T} + \tau_t E + \kappa_t(E-1.022)]}{\mu_t} \right\}_j , \quad (27)$$

where $\nu$ is the number of interactions in the target before history termination.

We score the central-axis quantity $F_S$ in a slightly different manner. Because the sphere is small the probability that a photon path will intersect the sphere is small. To improve the simulation efficiency, we find the solid angle subtended by the sphere at each interaction point in the shield and force scatters into this solid angle. This procedure is discussed in Appendix C. We then extend the path to the sphere, force an interaction there, and score the energy deposition with an estimator like that used for the cylinder. However, we do not continue the photon simulation through multiple interactions in the sphere, because of its small size. Rather, we return to the interaction point in the shield and continue simulation there. The sphere energy deposition estimator thus has the form

$$\Delta E_S = e^{-\mu\delta} W_\theta W_\phi [1 - e^{-\mu t^\delta t}] \frac{[\sigma_t^\overline{T} \tau_t E + \kappa_t(E-1.022)]}{\mu t} \tag{28}$$

where $W_\theta$ and $W_\phi$ are weight factors for forcing scatter toward the sphere and are defined in Appendix C.

We have not attempted to develop highly sophisticated dose descriptors that require use of materials more tissue-equivalent than water (for instance, as specified by the ICRU [14]) or that are truly dose-equivalent [15] or representative of actual dosimeter measurements, since these are unnecessary to study the gross effects of shield layering and placement. However, in studying the finer details of shield design, a more sophisticated target scoring scheme could be employed.

# IV. CODE VERIFICATION

## A.  General

We have verified the components of the code and its internal consistency
in various ways.  In general, the code was written in modular form and each
module separately tested and checked carefully before integration with the
rest of the code.  For instance, individual subroutines were written to find
the intersections of rays with planes, cylindrical surfaces and spheres (as
described in Appendix A) and each subroutine was tested before inclu~ ~n in
the code.  The subroutine to determine conditions following incoherent scatter
was verified by calling the subroutine repeatedly for the same initial photon
energy, plotting the frequency distribution of the resulting scattering angle
and comparing to the known distribution given by Evans [16].  The photon cross
section library was constructed by piecewise polynomial fit over the range 10
keV to 20 MeV to the data of Hubbell [17].  It was thoroughly tested and the
relative error between model and data was shown to be generally less than 3
percent.

The integrated code was also tested.  We have shown that gamma-ray
transport through two contiguous shield layers is identical to transport
through one layer of the same total thickness, as a partial check of the
geometry of treating layers.  We also ran several MC histories with a detailed
output of various intermediate variables which were checked independently
using a hand-calculator.

As a further check of the code, we have generated the various surface
quantities required in the inverse formulation of Siewert and Dunn [18] for a
monoenergetic, monodirectional beam incident at a point on the surface of a
single shield layer of radius 1000 cm and thickness 4 cm, approximating a
plane parallel medium of infinite radius.  Since this inverse solution assumes
isotropic scattering, we used the isotropic scattering option available in the
code, which keeps the Compton cross section at its value at the incident
gamma-ray energy and samples the cosine of the scatter angle from a uniform
distribution on (-1,1).  For this case, one form of the inverse solution can
be expressed [18]

29

$$c = \frac{\sigma}{\mu} = \frac{8\pi \ \psi(-\alpha_0, \phi_0)}{\psi_{\ell}^2 - \psi_r^2} \quad , \tag{1}$$

where $\sigma$ and $\mu$ are the Compton and total linear attenuation coefficients, respectively, $\alpha_0 > 0$ is the x-direction cosine of the incident beam, $\phi_0$ is the azimuthal angle of the incident beam measured positive CCW from the +z axis, $\psi(-\alpha_0, \phi_0)$ is the exit angular flux in the direction opposite the incident beam integrated over the entire left surface, $\psi_{\ell}$ is the total flux integrated over all directions over the entire left surface, and $\psi_r$ is the total flux integrated over all directions over the right surface. The required exit fluxes are found by a last flight estimator, where the estimator after each interaction (including initial entry to the shield) has the form

$$\phi = \frac{W \ e^{-\mu\Delta}}{|\zeta|} \quad , \tag{2}$$

where W is the incoming history weight, $\Delta$ the distance to the shield surface and $\zeta$ the cosine of the angle between the extended gamma-ray path and the outward normal to the shield surface at the exit point. Substituting the simulated quantities into Eq. 1, we have recovered the ratio of scattering to total cross sections at the energy of the incident gamma-rays to within one percent of the correct value. This check verifies the geometrical treatment of photon transport and the implementation of last-flight estimation.

# V. RESULTS

For our analysis we have chosen a standard target arrangement consisting of a one-meter diameter by one-meter long circular cylinder and a 5-cm diameter sphere located at the center of the cylinder. Both targets are assumed to consist of water, which is approximately tissue-equivalent. The cylinder is representative of a relatively large target within which multiple photon interactions may occur; the sphere is small enough that multiple photon interactions inside it are unlikely and that its dose is a reasonable measure of central-axis dose. The fractional energy absorbed per incident MeV, as discussed in Chapter III, is determined for each target, in the absence of the other.

The assumed photon spectrum is taken from Glasstone and Dolan [19], pp. 360-1, and is approximated by: $E_0 = 0$, $E_1 = 0.75$, $E_2 = 2$, $E_3 = 4.5$, $E_4 = 8$, $E_5 = 12$; $S_1 = 0.7$, $S_2 = 0.8$, $S_3 = 0.89$, $S_4 = 0.975$, $S_5 = 1$. We have chosen to treat three incident energy conditions: monoenergetic low, monoenergetic high and the full Glasstone and Dolan [19] spectrum. In this way low- and high-energy effects can be isolated initially for separate study and then considered in a composite manner at a later stage. The midpoint of the first energy interval, which contains 70 percent of the photons, is 0.375 MeV and so defines the low-energy case. The monoenergetic high case is taken as 2.5 MeV, which is the approximate weighted average of the remaining 30 percent of the spectrum.

It is well known that gamma radiation in a thin-beam geometry is attenuated exponentially. In broad-beam, thick-shield geometry, however, build-up occurs due to multiple scattering and the dose (or intensity) on the far side of the shield is larger than a strict exponential model of the form

$$D(T) = D_0 \, e^{-\mu T} \tag{1}$$

would predict. In Eq. 1 $D(T)$ denotes some dose measure at the far surface of the shield of thickness $T$, $D_0$ the same measure for $T = 0$ and $\mu$ the linear attenuation coefficient of the shield material. The ratio of actual dose to dose estimated by the simplified model of Eq. 1 is commonly called the dose buildup factor. This factor depends on shield material, photon energy and

shield thickness, but can be as large as 10 or 20 or even 100 [4,20] and tends to increase with increasing shield thickness. The fact that this buildup of dose can be so significant and that it is due to scattering in the shield beg investigation of the extent to which the scattered dose contribution can be reduced by modifying either the scattering process or the transport of photons between interactions. Various aspects of shield design are studied in the following sections.

### Effect of Shield Thickness

In Table V-1 we show the quantities $F_S$ and $F_C$ as functions of shield thickness for a shield composed of a single layer of lead positioned at various target-to-shield distances, d. The central sphere quantities, $F_S$, are plotted in Fig. V-1. Several things are apparent from these results. First of all, the variation of $F_S$ with thickness is approximately exponential at large thicknesses (straight lines on the semilogarithmic scale), especially for the low-energy cases (Cases 1, 2 and 3). However, for small thicknesses, the behavior is decidely not exponentially decreasing, especially for d = 0 (i.e., for the shield near the target), and even for large thicknesses the rate of decrease is much smaller than the attenuation rate of primary photons, $e^{-\mu T}$, where $\mu$ = 2.84 cm$^{-1}$ at 0.375 MeV and $\mu$ = 0.044 at 2.5 MeV (Cases a and b in Fig. V-1). In fact, at 2.5 MeV there is actually an increase in target dose for thin shields over the no-shield case, clearly pointing out the scattered-photon contribution.

From Table V-1 it is clear that the cylinder dose quantity, $F_C$, behaves similarly, although there is no increase in dose over the no-shield case for thin shields, even at 2.5 MeV. It is also obvious from these results that the farther the shield is from the target, the lower the dose. This effect will be investigated next.

### Effect of Target-to-Shield Distance

We now consider a single shield of fixed thickness, T, and study the effect on dose of where the shield is placed relative to the target. Several cases are considered in Table V-2 and Fig. V-2. At T = 2 mfp and $E_0$ = 0.375 MeV (Case 5) we see that a reduction in the quantity $F_S$ by almost a factor of three is possible simply by separating the shield from the cylinder

32

TABLE V-1. EFFECT OF SHIELD THICKNESS AT VARIOUS
TARGET-TO-SHIELD DISTANCES, d, FOR LEAD-SHIELD LAYERS

| Case No. | $E_0$ (MeV) | n | T (mfp) | T (cm) | d (cm) | $F_S$ (eV/MeV) | $F_C$ (keV/MeV) |
|---|---|---|---|---|---|---|---|
| 1 | 0.375 | 1 | 0 | 0 | 0 | 227.2 | 766.6 |
|   |       |   | 1 | 0.3525 | 0 | 199.6 | 310.3 |
|   |       |   | 2 | 0.705 | 0 | 101.7 | 172.0 |
|   |       |   | 4 | 1.41 | 0 | 18.9 | 16.4 |
|   |       |   | 8 | 2.82 | 0 | 0.5 | 0.2 |
| 2 | 0.375 | 1 | 0 | 0 | 200 | 227.2 | 766.6 |
|   |       |   | 1 | 0.3525 | 200 | 99.6 | 286.3 |
|   |       |   | 2 | 0.705 | 200 | 43.0 | 107.5 |
|   |       |   | 4 | 1.41 | 200 | 7.6 | 13.5 |
|   |       |   | 8 | 2.82 | 200 | 0.2 | 0.1 |
| 3 | 0.375 | 1 | 0 | 0 | 400 | 227.2 | 766.6 |
|   |       |   | 1 | 0.3525 | 400 | 89.3 | 294.6 |
|   |       |   | 2 | 0.705 | 400 | 35.2 | 105.6 |
|   |       |   | 4 | 1.41 | 400 | 5.4 | 13.1 |
|   |       |   | 8 | 2.82 | 400 | 0.1 | 0.1 |
| 4 | 2.5 | 1 | 0 | 0 | 0 | 191.3 | 888.9 |
|   |       |   | 1 | 2.065 | 0 | 310.1 | 409.3 |
|   |       |   | 2 | 4.13 | 0 | 204.5 | 178.9 |
|   |       |   | 4 | 8.26 | 0 | 48.4 | 30.5 |
|   |       |   | 8 | 16.52 | 0 | 6.7 | 0.7 |
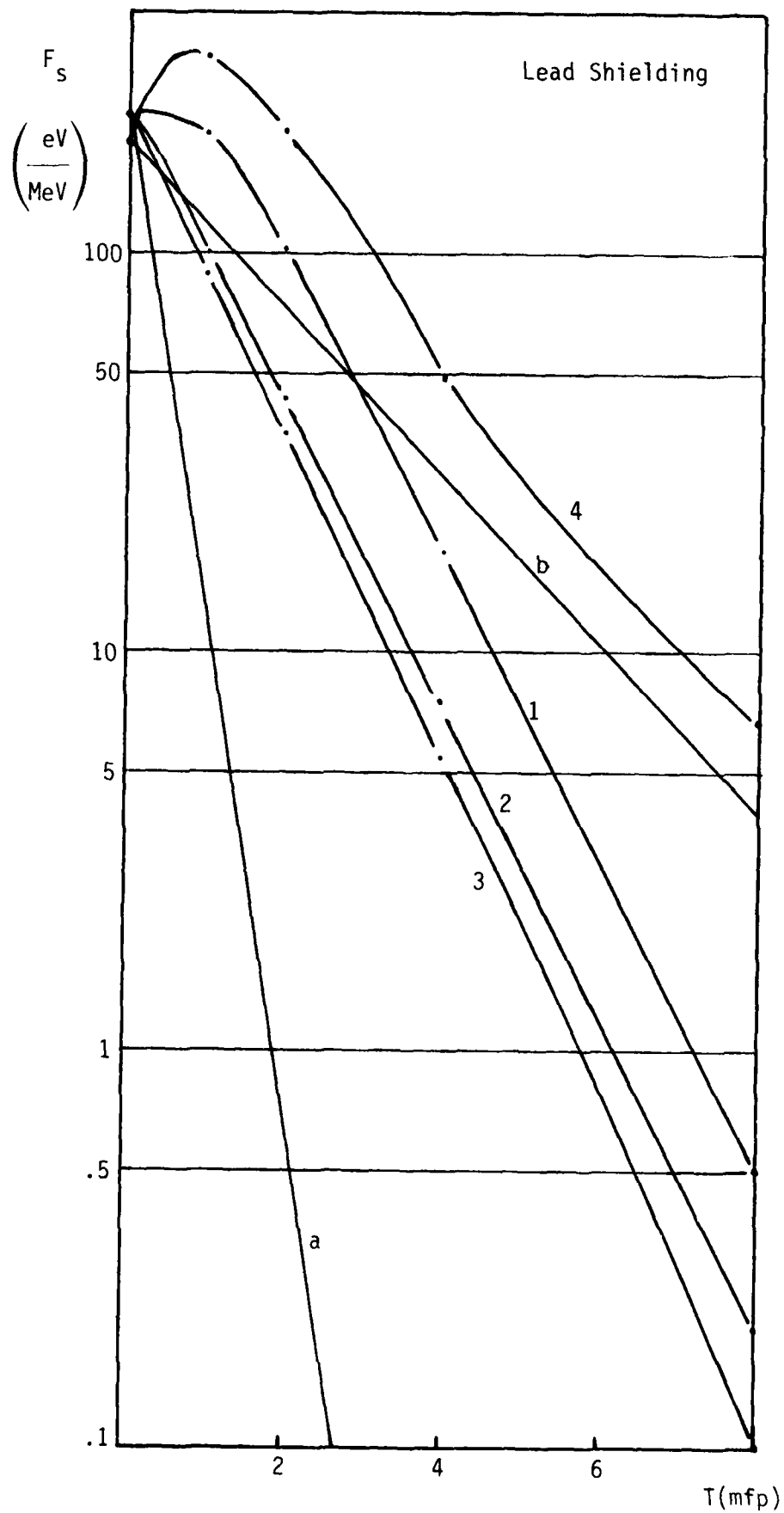
Figure V-1. Variation of Sphere Energy
Fraction with Shield Thickness

TABLE V-2.  EFFECT OF TARGET-TO-SHIELD DISTANCE, d,
FOR SINGLE-LAYER SHIELDS

| Case No. | $E_0$ (MeV) | n | T (mfp) | (cm) | d (cm) | $F_s$ (eV/MeV) | $F_c$ (keV/MeV) |
|---|---|---|---|---|---|---|---|

a. Lead Shielding

| Case No. | $E_0$ (MeV) | n | T (mfp) | (cm) | d (cm) | $F_s$ (eV/MeV) | $F_c$ (keV/MeV) |
|---|---|---|---|---|---|---|---|
| 5 | 0.375 | 1 | 2 | 0.705 | 0 | 101.7 | 122.0 |
|   |   |   |   |   | 100 | 58.2 | 111.6 |
|   |   |   |   |   | 200 | 43.0 | 107.5 |
|   |   |   |   |   | 300 | 37.8 | 105.7 |
|   |   |   |   |   | 400 | 35.2 | 105.6 |
| 6 | 0.375 | 1 | 4 | 1.41 | 0 | 18.9 | 16.4 |
|   |   |   |   |   | 40 | 16.6 | 15.2 |
|   |   |   |   |   | 80 | 12.6 | 14.6 |
|   |   |   |   |   | 100 | 11.6 | 14.5 |
|   |   |   |   |   | 200 | 7.6 | 13.5 |
|   |   |   |   |   | 300 | 6.1 | 13.5 |
|   |   |   |   |   | 400 | 5.4 | 13.1 |
| 7 | 2.5 | 1 | 4 | 8.26 | 0 | 48.4 | 30.5 |
|   |   |   |   |   | 40 | 49.3 | 26.5 |
|   |   |   |   |   | 80 | 42.9 | 25.1 |
|   |   |   |   |   | 100 | 37.9 | 23.6 |
|   |   |   |   |   | 200 | 22.4 | 19.7 |
|   |   |   |   |   | 300 | 15.7 | 17.8 |
|   |   |   |   |   | 400 | 12.0 | 17.4 |

b. Water Shielding

| Case No. | $E_0$ (MeV) | n | T (mfp) | (cm) | d (cm) | $F_s$ (eV/MeV) | $F_c$ (keV/MeV) |
|---|---|---|---|---|---|---|---|
| 8 | 0.375 | 1 | 2 | 18.4 | 0 | 475.1 | 212.3 |
|   |   |   |   |   | 100 | 206.4 | 131.9 |
|   |   |   |   |   | 200 | 125.1 | 114.3 |
|   |   |   |   |   | 400 | 77.7 | 108.1 |
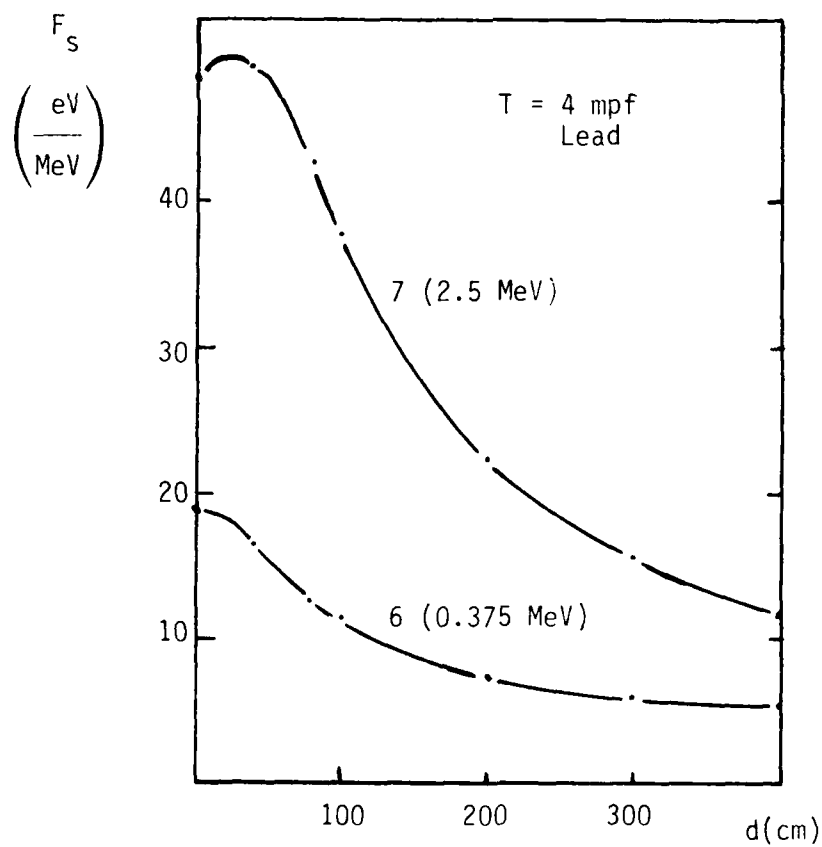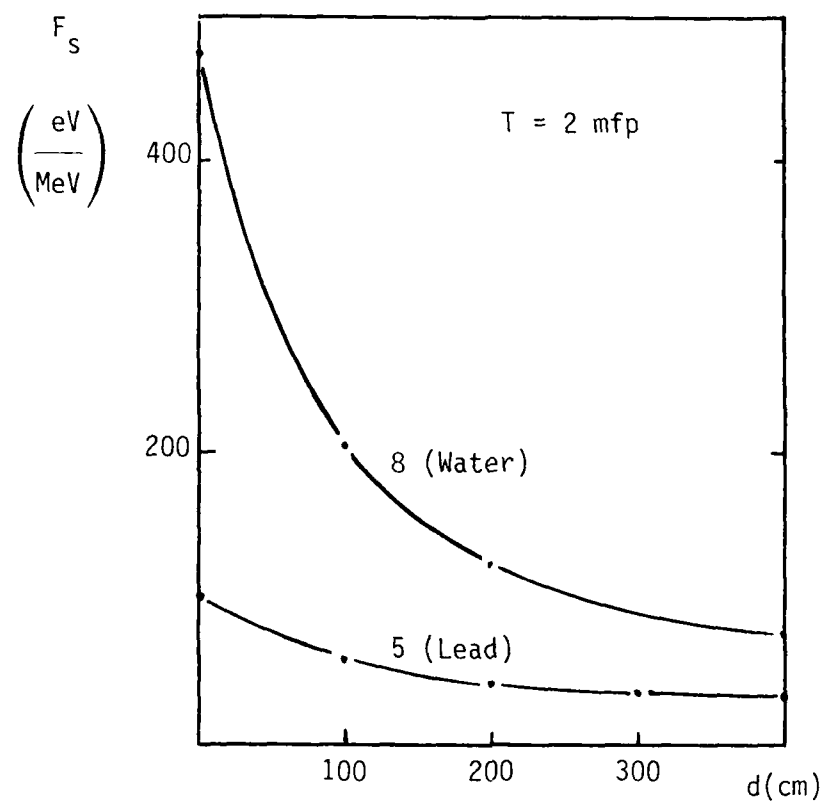
Figure V-2.  Variation of Sphere Energy
Fraction with Target-to-Shield Distance

36

target from 0 to 4 meters. At 4 mfp (Case 6) the reduction is greater than a factor of three. This effect is exaggerated at higher energies (in Case 7 the reduction is a factor of four), presumably because of the approximate isotropy of annihilation interactions as opposed to the forward-biased scattering of Compton interactions.

Case 8 in Table V-2 shows that while the absolute doses are considerably larger for a low-Z, water shield of 2 mfp thickness the effect of target-to-source distance is significantly increased, with the ratio $F_S(d = 0)/F_S(d = 4m)$ being greater than 6. This is presumably due to the fact that hydrogen is a more effective Compton scatterer than other elements, since $\sigma \alpha Z/A$ and $Z/A \simeq 0.5$ for all elements except hydrogen for which $Z/A \simeq 1$ (here Z is atomic number and A atomic weight). This suggests that a shield that includes hydrogen (as in a polymer) at large D to induce scattering and then a high density material (such as steel or lead) to provide high attenuation might be more effective than a strictly high-Z shield of equal mass. We note also that such a configuration is ideal for shielding against neutrons (the hydrogen-rich layer would thermalize the neutrons which could then be absorbed by a thin layer of cadmium or of borated or rare-earth doped material).

### Effect of Layering

The effect of layering cannot be directly isolated from the effect of target-to-shield separation, since any splitting of a shield into noncontiguous layers necessarily changes the target-to-shield separation for at least one of the layers. Thus, we consider various aspects of shield layering separately. First, we show in Table V-3 the dependence of $F_S$ and $F_C$ on spacing, S, for a shield split into two layers with the first layer at constant d. Cases 9 and 10 ($E_0 = 0.375$ MeV) demonstrate the general dose decrease with increasing S; whether the first layer is close to or removed from the target, there is an approximately 20 percent decrease in $F_S$ in going from S = 0 (effectively, one thick shield) to S = 3 m. These results indicate that the effectiveness of layering tends to decrease as d increases but that the overall shield effectiveness improves. Case 11 shows that the effect is greater at 2.5 MeV and Cases 12 and 13 show that the effect is much greater for water than lead. The results are plotted in Fig. V-3.

TABLE V-3.  EFFECT OF SPLITTING SHIELD INTO 2 LAYERS (n = 2)

| Case No. | $E_0$ (MeV) | S (cm) | T (mfp) | D (cm) | d (cm) | $F_s$ (eV/MeV) | $F_c$ (keV/MeV) |
|---|---|---|---|---|---|---|---|
| **a.  Lead Shielding** | | | | | | | |
| 9 | 0.375 | 0 | 4 | 1.41 | 0 | 18.9 | 16.4 |
|  |  | 98.59 | 4 | 100 | 0 | 16.7 | 15.7 |
|  |  | 198.59 | 4 | 200 | 0 | 15.0 | 13.5 |
|  |  | 298.59 | 4 | 300 | 0 | 15.1 | 15.6 |
| 10 | 0.375 | 0 | 4 | 201.41 | 200 | 7.6 | 13.5 |
|  |  | 98.59 | 4 | 300 | 200 | 6.8 | 13.3 |
|  |  | 198.59 | 4 | 400 | 200 | 6.4 | 13.4 |
|  |  | 298.59 | 4 | 500 | 200 | 6.2 | 13.3 |
| 11 | 2.5 | 0 | 4 | 208.26 | 200 | 22.4 | 19.7 |
|  |  | 191.74 | 4 | 400 | 200 | 15.9 | 18.6 |
|  |  | 291.74 | 4 | 500 | 200 | 14.4 | 17.9 |
| 12 | 0.375 | 0 | 2 | 400.705 | 400 | 35.2 | 105.6 |
|  |  | 199.295 | 2 | 600 | 400 | 33.9 | 104.6 |
|  |  | 399.295 | 2 | 800 | 400 | 33.4 | 104.6 |
| **b.  Water Shielding** | | | | | | | |
| 13 | 0.375 | 0 | 2 | 418.4 | 400 | 77.7 | 108.1 |
|  |  | 181.6 | 2 | 600 | 400 | 55.3 | 106.3 |
|  |  | 381.6 | 2 | 800 | 400 | 51.7 | 104.9 |
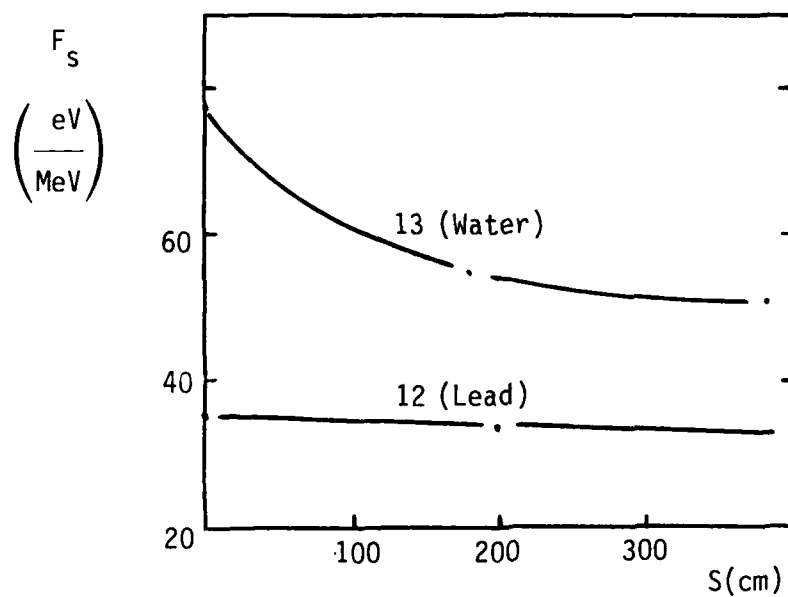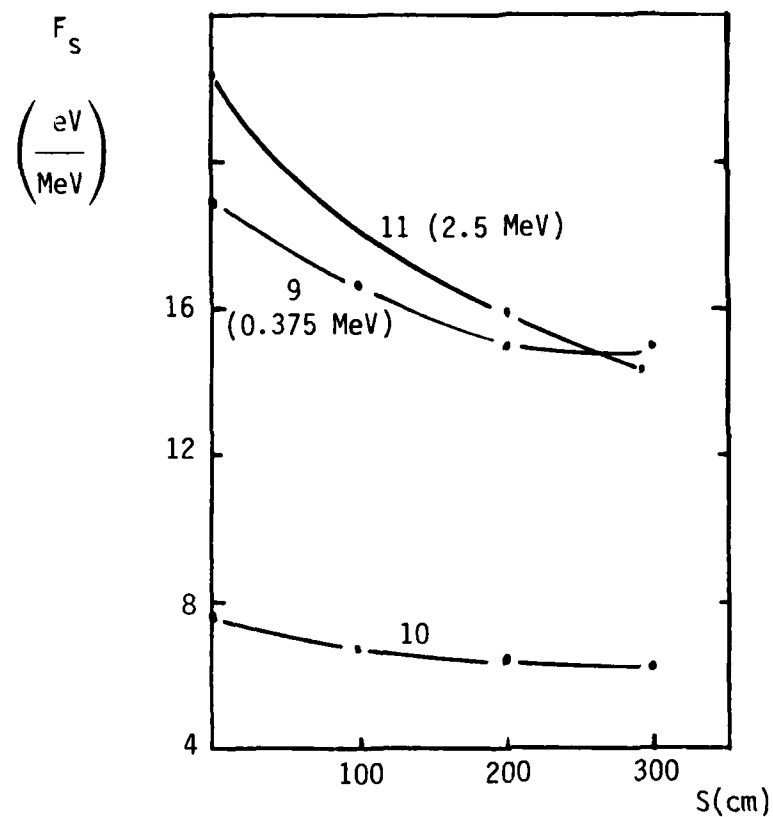
Figure V-3.   Variation of Sphere Energy
Fraction with Spacing Between Two Layers

The effect of splitting into many layers is indicated in Table V-4 and Fig. V-4. Case 14 is for constant spacing between layers, $S/(n - 1)$, while Cases 14 and 16 allow the spacing between layers to decrease with increasing n. It is apparent that the effect is again greater for high energy, but significant for both low and high. We note that the reduction with n would be greater in Cases 15 and 16 if $S/(n - 1)$ were constant at 200 cm. As a contrived means to study the effect in the limit as $n \to \infty$, we ran a case in which we spread an hypothetical lead shield over a 2-m distance and lowered the density, to keep the mass constant. This result supports the conclusion that for fixed d and D (i.e., under constraints on minimum and maximum target-to-shield separations), there is little gain in splitting into more than about 4 layers, i.e., although layering always helps, its marginal improvement is small after about $n = 4$ layers.

### Effect of Thickness Gradient

We have shown that layering (including the effects of varying D) can lead to substantial dose reduction (e.g., greater than a factor of 2 in Case 15). We now wish to investigate the prospects for dose reduction under the constraint, likely to be encountered in actual shielding situations, that both d and D are constrained, i.e., the distance from the target to the first (farthest) shield cannot exceed some limiting value. The results of this study are shown in Table V-5, and are quite impressive. Case 17 demonstrates that at 0.375 MeV an 11 percent decrease in $F_S$ results when the relative proportion of shield thicknesses is changed from 1:1:2 to 2:1:1, with the shield members at the same locations in the two cases. At 2.5 MeV (Case 18), this decrease is almost 25 percent for the same proportionate thickness change and is greater than 42 percent in going from thickness proportions 1:1:2 to 6:2:1. The effect is similarly impressive for water shields (Case 19), as expected. Hence, it appears that rather substantial reductions in central-axis dose are possible, even when structural or other constraints dictate that part of the shield must be positioned close to the target.

TABLE V-4. EFFECT OF SPLITTING INTO MANY LAYERS

| Case No. | $E_0$ (MeV) | n | $\dfrac{S}{n-1}$ | T (mfp) | D (cm) | d (cm) | $F_s$ (eV/MeV) | $F_c$ (keV/MeV) |
|---|---|---|---|---|---|---|---|---|
| 14 | 0.375 | 1 | - | 4 | 201.41 | 200 | 7.6 | 13.5 |
|  |  | 2 | 200 | 4 | 400 | 200 | 6.4 | 13.4 |
|  |  | 4 | 200 | 4 | 800 | 200 | 5.4 | 13.2 |
|  |  | 6 | 200 | 4 | 1200 | 200 | 5.0 | 13.1 |
|  |  | 8 | 200 | 4 | 1600 | 200 | 4.9 | 13.0 |
| 15 | 2.5 | 1 | - | 4 | 208.26 | 200 | 22.4 | 19.7 |
|  |  | 2 | 200 | 4 | 400 | 200 | 15.9 | 18.6 |
|  |  | 4 | 133 | 4 | 600 | 200 | 11.4 | 17.3 |
|  |  | 8 | 114 | 4 | 1000 | 200 | 8.7 | 17.0 |
| 16 | 0.375 | 1 | - | 4 | 1.41 | 0 | 18.9 | 16.4 |
|  |  | 2 | 200 | 4 | 200 | 0 | 15.0 | 13.5 |
|  |  | 4 | 50 | 4 | 200 | 0 | 14.2 | 15.1 |
|  |  | $\infty$* | 0 | 4 | 200 | 0 | 13.7 | 15.1 |

* A hypothetical lead shield of thickness 200 cm, density 0.079947 $gm/cm^3$, was modeled, having the same total mass (125.58 kg) as the 1.41 cm shield with normal density 11.34 $gm/cm^3$. This simulates the stretching out of the shield into an infinite number of layers.
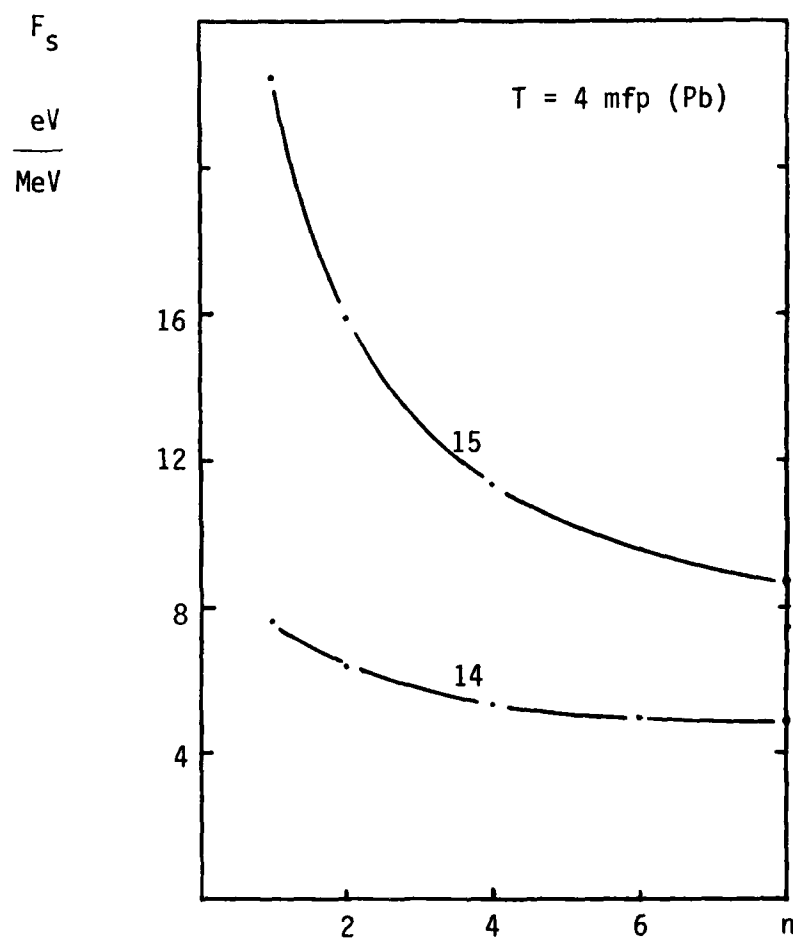
Figure V-4.  Variation of Sphere Energy
Fraction with Number of Layers

## TABLE V-5. EFFECT OF THICKNESS GRADIENT;
### d = 200 cm, D ≈ 800 cm, n = 3

| Case No. | E (MeV) | $t_1$ (cm) | $t_2$ (cm) | $t_3$ (cm) | $F_s$ (eV/MeV) | $F_c$ (keV/MeV) |
|---|---|---|---|---|---|---|
| a. Lead Shielding, T = 1.41 (4 mfp) | | | | | | |
| 17 | 0.375 | .3525 | .3525 | .705 | 6.1 | 13.3 |
| | | .282 | .564 | .564 | 5.7 | 13.5 |
| | | .470 | .470 | .470 | 5.6 | 13.1 |
| | | .705 | .3525 | .3525 | 5.4 | 13.2 |
| 18 | 2.5 | 2.065 | 2.065 | 4.13 | 13.3 | 18.3 |
| | | 1.652 | 3.304 | 3.304 | 11.9 | 17.6 |
| | | 2.7534 | 2.7533 | 2.7533 | 10.9 | 17.4 |
| | | 4.13 | 2.065 | 2.065 | 10.0 | 17.7 |
| | | 5.509 | 1.834 | 0.917 | 7.6 | 16.7 |
| b. Water Shielding, T = 18.4 cm | | | | | | |
| 19 | 0.375 | 4.6 | 4.6 | 9.2 | 70.1 | 108.6 |
| | | 6.134 | 6.133 | 6.133 | 56.6 | 106.6 |
| | | 9.2 | 4.6 | 4.6 | 53.0 | 107.4 |

43

### Effects for the Whole-Spectrum Case

The results presented so far were for monoenergetic incident photons. We view typical cases in both the simplified and generalized geometries in Table V-6 for the Glasstone and Dolan [19] spectrum. Here, the sharp decrease of $F_S$ and $F_C$ with increasing source-to-closest-layer distance, d, is evident in Case 20, plotted in Fig. V-5a, and the substantial decrease with increasing number of layers (for constant d) is clear from Case 21, shown in Fig. V-5b. The effect of reducing the thickness of the layer nearest the target to reduce dose is obvious from Case 22.

### Effects of a Diverging Incident Beam

The results of Table V-7 indicate that the dose reduction effects are similar for a diverging as opposed to a parallel beam. In general, the trends are similar in the two cases, but the dose quantities for the diverging case are approximately 80-90 percent of those for the parallel case, as expected. The specific case considered involved significant divergence, since the source was assumed to be only 100 m from the front of the cylindrical target. Thus, we conclude that for beams typical of remote bursts or directed energy weapons (which should be bounded by the parallel- and divergent-beam cases considered here), the effects of layering, thickness gradients and shield geometry are quite significant.

TABLE V-6. RESULTS FOR INCIDENT PHOTONS DISTRIBUTED
ACCORDING TO THE GLASSTONE AND DOLAN [19] SPECTRUM

| Case No. | n | T (cm) | D (cm) | d (cm) | $F_S$ (eV/MeV) | $F_C$ (keV/MeV) |
|---|---|---|---|---|---|---|

a. Dependence on d and n, Simplified Geometry

| Case No. | n | T (cm) | D (cm) | d (cm) | $F_S$ (eV/MeV) | $F_C$ (keV/MeV) |
|---|---|---|---|---|---|---|
| 20 | 1 | 3 | 3 | 0 | 122.4 | 186.7 |
|    |   |   | 103 | 100 | 100.9 | 169.1 |
|    |   |   | 203 | 200 | 66.9 | 161.1 |
|    |   |   | 303 | 300 | 51.7 | 156.2 |
|    |   |   | 403 | 400 | 44.2 | 154.4 |
| 21 | 1 | 3 | 203 | 200 | 66.9 | 161.1 |
|    | 2 |   | 400 | 200 | 53.7 | 156.7 |
|    | 4 |   | 600 | 200 | 47.1 | 157.1 |
|    | 4 |   | 800 | 200 | 41.5 | 156.5 |
|    | 8 |   | 1000 | 200 | 38.9 | 153.1 |
|    | 8 |   | 1600 | 200 | 35.4 | 152.6 |

b. Effect of Thickness Gradient, d = 200 cm, D = 800 cm, Generalized Geometry

| Case No. | n | t1 (cm) | t2 (cm) | t3 (cm) | $F_S$ (eV/MeV) | $F_C$ (keV/MeV) |
|---|---|---|---|---|---|---|
| 22 | 3 | 1.6 | 1.2 | 1.2 | 45.4 | 158.4 |
|    | 3 | 1 | 1 | 1 | 43.0 | 154.2 |
|    | 3 | 2 | .5 | .5 | 38.2 | 153.6 |

45
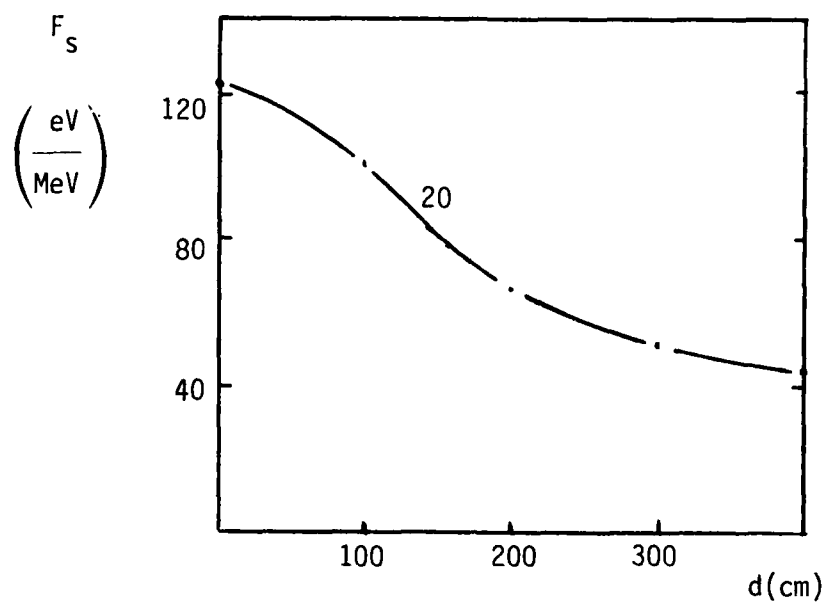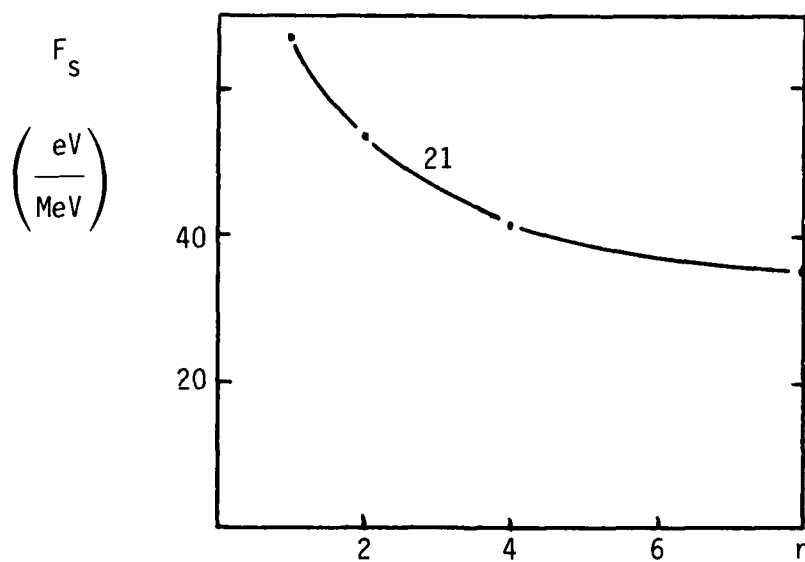
(a)  Variation with d



(b)  Variation with n

Figure V-5.  Sphere Energy Fraction for the
Whole-Spectrum Case

46

TABLE V-7. RESULTS FOR DIVERGENT INCIDENT BEAM FOR THE
SOURCE-TO-TARGET DISTANCE = 100 m

| Case No. | n | T (cm) | D (cm) | d (cm) | $F_s$ (eV/MeV) | $F_c$ (keV/MeV) |
|----------|---|--------|--------|--------|----------------|-----------------|

a. Dependence on n, Simplified Geometry

| Case No. | n | T (cm) | D (cm) | d (cm) | $F_s$ (eV/MeV) | $F_c$ (keV/MeV) |
|----------|---|--------|--------|--------|----------------|-----------------|
| 23 | 1 | 0 | 0 | 0 | 168.1 | 828.5 |
|    | 1 | 3 | 203 | 200 | 58.0 | 153.3 |
|    | 2 | 3 | 400 | 200 | 43.5 | 145.5 |
|    | 4 | 3 | 800 | 200 | 34.0 | 134.2 |

b. Effect of Thickness Gradient, d = 200 cm, D = 800 cm, Generalized Geometry

| Case No. | n | $t_1$ (cm) | $t_2$ (cm) | $t_3$ (cm) | $F_s$ (eV/MeV) | $F_c$ (keV/MeV) |
|----------|---|------------|------------|------------|----------------|-----------------|
| 24 | 3 | .75 | .75 | 1.5 | 37.9 | 128.2 |
|    | 3 | 1 | 1 | 1 | 34.6 | 132.3 |
|    | 3 | 1.5 | .75 | .75 | 31.3 | 131.6 |

## VI. CONCLUSIONS

This Phase I study draws attention to the importance of geometric optimization in shielding both terrestrial and space vehicles against directed gamma-ray beams. By means of a versatile and efficient Monte Carlo model developed for this purpose, it has been shown that doses to the target may be reduced by factors of 2 or 3 without increase in shield mass, through careful choice of shield configuration; alternatively, for a given acceptable dose, the shield mass may be considerably reduced. The tremendous influence of target-shield geometry has been demonstrated and the effects of target-to-nearest-l, distance, layer spacing, number of layers and layer thickness gradient have been quantified. The studies to date also indicate promising areas for further improvements. Composition gradients, wherein light-weight, effective-scattering materials would be placed farthest from the target (to convert the highly-monodirectional incident beam into a more dispersed beam) and subsequent layers would be included for gamma-ray (and neutron) absorption, should be effective. The dependence on lateral dimensions and non-idealized geometries has not yet been investigated.

The main conclusions to be drawn are the following: (1) target configuration plays a major role in determining shield effectiveness; (2) apparently minor geometric effects (e.g., transferring small thicknesses from one layer to another) can have surprisingly significant effects on target dose; and (3) the dose distribution over a large target volume is not uniformly modified by layering, i.e., a shield mass capable of achieving only modest overall dose reduction may, by geometric means, provide adequate shielding for particular, vulnerable locations. The objectives of the Phase I study: (1) to develop a suitable formalism and (2) to demonstrate the importance of geometric optimization in a limited number of moderately simple cases, have been fully realized. In a Phase II submittal it is proposed to apply the principles already demonstrated to much more complex designs which can be used in mixed neutron-gamma fields and in cases where shielding is required over a solid angle approaching a half-space.

## VII. REFERENCES

1. R. E. Lapp and H. L. Andrews, Nuclear Radiation Physics, Fourth Edition, Prentice-Hall, Inc., Englewood Cliffs, New Jersey, p. 233, 1948.

2. H. E. Johns, and J. R. Cunningham, The Physics of Radiology, Fourth Edition, Charles C. Thomas, Springfield, Illinois, p. 139 ff, 1983.

3. A. Macovski, Medical Imaging, Prentice-Hall, Inc., Englewood Cliffs, New Jersey, p. 91 ff, 1983.

4. B. T. Price, C. C. Horton and K. T. Spinney, Radiation Shielding, Pergamon Press, New York, New York, p. 40, 1957.

5. W. L. Dunn, "Inverse Monte Carlo Analysis," J. Comput. Phys. 41:154, 1981.

6. W. L. Dunn, "Inverse Monte Carlo Solutions for Radiative Transfer in Inhomogeneous Media," J. Quant. Spectrosc. Radiat. Transfer 29(1):19, 1983.

7. W. L. Dunn and F. O'Foghludha, "Feasibility Studies for Design of Photon Beam Modifiers Using Monte Carlo Methods," Proc. of the World Congress on Medical Physics and Biomedical Engineering, Hamburg, September 1982.

8. H. Kahn, "Application of Monte Carlo," (AECU-3259, U.S. Atomic Energy Commission), The Rand Corporation, Santa Monica, California, 1956.

9. L. L. Carter and E. D. Cashwell, Particle Transport Simulation with the Monte Carlo Method, ERDA Critical Review Series, TID-26607, NTIS, Springfield, Virginia, 1975.

10. R. V. Rubinstein, Simulation and the Monte Carlo Method, John Wiley & Sons, New York, New York, 1981.

11. W. E. Selph and C. W. Garrett, "Monte Carlo Methods for Radiation Transport," pp. 207-59 in Reactor Shielding for Nuclear Engineers, (N. M. Schaeffer, Ed.), USAEC, TID-25951, NTIS, Springfield, Virginia, 1973.

12. E. J. McGrath and D. C. Irving, "Techniques for Efficient Monte Carlo Simulation, Volume III, Variance Reduction," ORNL-RSIC-38, Oak Ridge, Tennessee, 1975.

13. W. L. Dunn and R. P. Gardner, "The Determination of Intrinsic Gamma-Ray Detection Efficiencies for Cylindrical Geiger-Muller Tubes by Monte Carlo Methods," Nuc. Instr. Meth. 103:373, 1972.

14. International Commission on Radiation Units and Measurements, "Radiation Quantitites and Units," ICRU Report 19, ICRU Publications, Washington, D.C., 1971.

15. M. Hoefert, G. R. Stevenson and C. Yamaguchi, "On the Determination of Dose Equivalent for Photons of Energies Between 4 and 10 MeV," Health Phys. 46(2):476, 1984.

16. R. D. Evans, The Atomic Nucleus, McGraw-Hill Book Company, New York, New York, 1955.

17. J. H. Hubbell, "Photon Cross Sections, Attenuation Coefficients, and Energy Absorption Coefficients from 10 keV to 100 GeV," NSRDS-NBS-29, U.S. Department of Commerce, 1969.

18. C. E. Siewert and W. L. Dunn, "On Inverse Problems for Plane-Parallel Media with Nonuniform Surface Illumination," J. Math. Phys. 23(7):1376, 1982.

19. S. Glasstone and P. J. Dolan (Eds.), The Effects of Nuclear Weapons, U.S. Department of Defense and U.S. Department of Energy, Third Edition, 1977.

20. R. L. Murray, Introduction to Nuclear Engineering, Prentice-Hall, Inc., Englewood Cliffs, New Jersey, p. 260, 1961.

# APPENDIX A

## INTERSECTIONS OF GAMMA-RAY PATHS WITH SHIELD AND TARGET BOUNDARIES

### Ray to Plane

The planes are all $x$ = constant surfaces with $r < R$, where $R$ is the radius of the shield layer or target cylinder. If $\alpha = 0$, the ray is parallel to the plane and there is no intersection. Otherwise, we set

$$x_c = X_{i2} \quad , \; \alpha > 0 \qquad \qquad \text{(A-1a)}$$

$$x_c = X_{i1} \quad , \; \alpha < 0 \quad , \qquad \qquad \text{(A-1b)}$$

where i is the number of the shield layer that the photon position $(x,y,z)$ is in. Then, we must find the point $(x_c, y_c, z_c)$ where the line

$$\frac{x_c - x}{\alpha} = \frac{y_c - y}{\beta} = \frac{z_c - z}{\gamma} \qquad \qquad \text{(A-2)}$$

intersects the plane

$$x = x_c \quad , \qquad \qquad \text{(A-3)}$$

which, for $\alpha \neq 0$, is obviously

$$y_c = y + \frac{\beta}{\alpha} (x_c - x) \qquad \qquad \text{(A-4a)}$$

$$z_c = z + \frac{\gamma}{\alpha} (x_c - x) \quad . \qquad \qquad \text{(A-4b)}$$

We also calculate the radial distance to the intersection point,

$$r_c = [y_c^2 + z_c^2]^{1/2} \qquad \qquad \text{(A-5)}$$

and check to see if $r_c < R$. If not, the photon intersects the cylindrical surface before reaching the planar surface.

### Ray to Cylinder

The cylindrical surfaces are of the form

$$y_c^2 + z_c^2 = R^2 \quad , \qquad \qquad \text{(A-6a)}$$

with

$$X_{i1} \leq x \leq X_{i2} \quad . \tag{A-6b}$$

The target cylinder is treated like a shield layer with $i = n + 1$, where n is the number of layers. There are in general two intersections of the straight line of Eq. A-2 with the cylindrical surface of Eq. A-6. If $\gamma \neq 0$, these are given by

$$z_C = \frac{-B \pm [B^2 - 4AC]^{1/2}}{2A} \quad , \tag{A-7}$$

where

$$A = 1 + \left(\frac{\beta}{\gamma}\right)^2 \tag{A-8}$$

$$B = 2\frac{\beta}{\gamma}\left[y - \frac{\beta}{\gamma}z\right] \tag{A-9}$$

and

$$C = y^2 + \frac{\beta}{\gamma}z\left[\frac{\beta}{\gamma}z - 2y\right] - R^2 \quad . \tag{A-10}$$

If $\gamma > 0$, then $z_C > z$; if $\gamma < 0$, then $z_C < z$. Thus, we choose the solution for which $(z_C - z)/\gamma \geq 0$. Once $z_C$ is known, we then calculate

$$x_C = x + \frac{\alpha}{\gamma}(z_C - z) \tag{A-11a}$$

and

$$y_C = y + \frac{\beta}{\gamma}(z_C - z) \quad . \tag{A-11b}$$

For the case $\gamma = 0$ and $\beta \neq 0$, we use

$$y_C = \frac{-B \pm [B^2 - 4AC]^{1/2}}{2A} \tag{A-12}$$

with

52

$$A = 1 + \left(\frac{\gamma}{\beta}\right)^2 \qquad \text{(A-13)}$$

$$B = 2 \frac{\gamma}{\beta} \left[ z - \frac{\gamma}{\beta} y \right] \qquad \text{(A-14)}$$

and

$$C = z^2 + \frac{\gamma}{\beta} y \left[ \frac{\gamma}{\beta} y - 2z \right] \qquad \text{(A-15)}$$

and pick the solution for which $(y_c - y)/\beta \geq 0$. We then compute

$$x_c = x + \frac{\alpha}{\beta} (y_c - y) \qquad \text{(A-16a)}$$

$$z_c = z + \frac{\gamma}{\beta} (y_c - y) \quad . \qquad \text{(A-16b)}$$

If $\gamma = 0$ and $\beta = 0$, there is no solution. If $x_c > X_{12}$ or $x_c < X_{11}$, the ray exits the planar ends before reaching the cylindrical surface.

### Ray to Sphere

A sphere of radius $R_s$ centered at $(X_s, 0, 0)$ can be represented by

$$(x_c - X_s)^2 + y_c^2 + z_c^2 = R_s^2 \quad . \qquad \text{(A-17)}$$

For all cases of interest to us, $x$ will be less than $x_c$, since the shield layers are all to the left of the target central sphere. If $\alpha \leq 0$, there will thus be no intersection.

If $\alpha > 0$, we find again two possible solutions,

$$x_c = \frac{-B \pm [B^2 - 4AC]^{1/2}}{2A} \quad , \qquad \text{(A-18)}$$

where

$$A = \frac{1}{\alpha^2} \qquad \text{(A-19)}$$

$$B = 2 \left[ \frac{\beta y + \gamma z}{\alpha} - \frac{\beta^2 + \gamma^2}{\alpha^2} x - X_s \right] \qquad \text{(A-20)}$$

and

$$C = X_s^2 + y^2 + z^2 - 2x \left( \frac{\beta y + \gamma z}{\alpha} \right) + \frac{\beta^2 + \gamma^2}{\alpha^2} x^2 - R_s^2 \quad . \qquad \text{(A-21)}$$

If $B^2 - 4AC < 0$, there are no solutions and the ray does not intersect the sphere. If $B^2 - 4AC = 0$, there is only one solution and the ray is tangent to the sphere. If $B^2 - 4AC > 0$, there are two solutions and we take the one for which $x_c - $ is smaller. Then we find

$$y_c = y + \frac{\beta}{\alpha} (x_c - x) \qquad \text{(A-22a)}$$

and

$$z_c = z + \frac{\gamma}{\alpha} (x_c - x) \quad . \qquad \text{(A-22b)}$$

# APPENDIX B

## AVERAGE ENERGY LOST IN COMPTON COLLISION

There is a one-to-one correspondence between the energy of the scattered photon, $h\nu'$, and the scatter angle, $\theta$, in the Compton collision of a photon of energy $h\nu$ and a free electron; according to Evans [16] this relation can be written

$$h\nu' = \frac{m_0 c^2}{1 - \cos\theta + \frac{m_0 c^2}{h\nu}} \quad , \tag{B-1}$$

where $m_0 c^2 = 0.511$ MeV is the electron rest mass energy. We let $\eta$ be the incoming photon energy in units of $m_0 c^2$, i.e.,

$$\eta = \frac{h\nu}{m_0 c^2} \tag{B-2}$$

and define the reduced energy variable

$$\delta = \frac{h\nu}{h\nu'} \quad . \tag{B-3}$$

Then Eq. B-1 can be written in the form

$$\delta = 1 + \eta(1 - \cos\theta) \tag{B-4}$$

or its inverse

$$\cos\theta = \frac{\eta + 1 - \delta}{\eta} \quad . \tag{B-5}$$

The Klein-Nishina differential scattering formula for unpolarized incident radiation is given by Evans [16] as

$$d(_e\sigma) = \frac{r_0^2}{2} \left(\frac{\nu'}{\nu}\right)^2 \left[\frac{\nu}{\nu'} - \frac{\nu'}{\nu} - \sin^2\theta\right] 2\pi \sin\theta \, d\theta \quad , \tag{B-6}$$

55

where $r_0$ is the classical electron radius. Equation B-6 gives the probability that a photon of energy $h\nu$ will scatter within $d\theta$ about $\theta$ with final energy $h\nu'$ and has the form $d(_e\sigma) = f(\theta) \sin\theta\, d\theta$. We can rewrite Eq. B-6 in terms of $\delta$, obtaining

$$d(_e\sigma) = \frac{\pi r_0^2}{\delta^2} \left[ \delta + \frac{1}{\delta} - \sin^2\theta \right] \sin\theta\, d\theta \quad . \tag{B-7}$$

Because of the correspondence between $\delta$ and $\theta$, given $\eta$, expressed in Eqs. B-4 and B-5, we can write

$$d(_e\sigma) = f(\theta) \sin\theta\, d\theta = g(\delta|\eta)d\delta \quad , \tag{B-8}$$

from which we obtain

$$g(\delta|\eta) = f(\theta) \sin\theta \frac{d\theta}{d\delta} = -f(\theta) \frac{d\cos\theta}{d\delta} \tag{B-9a}$$

or

$$g(\delta|\eta) = \frac{\pi r_0^2}{\eta} \frac{1}{\delta^2} \left[ \delta + \frac{1}{\delta} - 1 + \left( \frac{\eta + 1 - \delta}{\eta} \right)^2 \right] \quad . \tag{B-9b}$$

Equation B-9b is a restatement of the Klein-Nishina scattering formula which, when normalized, gives the probability density function for $\delta$ given $\eta$.

The energy lost in a Compton collision is transferred to the struck electron; the energy of the secondary electron is thus [16]

$$T = h\nu - h\nu' \quad , \tag{B-10a}$$

which can be written in terms of $\delta$ as

$$T = h\nu \left( 1 - \frac{1}{\delta} \right) . \tag{B-10b}$$

We want the average energy lost per Compton collision, which is given by

$$\bar{T} = \frac{\int_{\delta_0}^{\delta_1} T(\delta)g(\delta|\eta)d\eta}{\int_{\delta_0}^{\delta_1} g(\delta|\eta)d\eta} = \frac{N}{D} \quad , \tag{B-11}$$

where, by Eq. B-4

$$\delta_0 = \delta(\theta = 0) = 1 \qquad (B-12a)$$

and

$$\delta_1 = \delta(\theta = \pi) = 1 + 2\eta \quad . \qquad (B-12b)$$

Performing the integrations in Eq. B-11, we obtain

$$N = \frac{h\nu \, \pi r_0^2}{\eta} \left\{ \frac{\eta^2 - 2\eta - 3}{\eta^2} \ln(1 + 2\eta) + \frac{4}{\eta} - \frac{2\eta^2 - 2\eta - 2}{\eta(1 + 2\eta)} + \frac{2\eta(1 + \eta)}{(1 + 2\eta)^2} \right.$$
$$\left. - \frac{2\eta(4\eta^2 + 6\eta + 3)}{3(1 + 2\eta)^3} \right\} \qquad (B-13)$$

and

$$D = \frac{\pi r_0^2}{\eta} \left\{ \frac{\eta^2 - 2\eta - 2}{\eta^2} \ln(1 + 2\eta) + \frac{4}{\eta} + \frac{2\eta(1 + \eta)}{(1 + 2\eta)} \right\} \quad . \qquad (B-14)$$

57

# APPENDIX C

## METHOD TO FORCE SCATTER TOWARD CENTRAL SPHERE

A photon with incoming direction $\hat{\Omega} = (\alpha,\beta,\gamma)$ interacts in the shield at position $(x,y,z)$. We wish to force a scatter into the solid angle subtended by the target sphere, centered at $(X_S,0,0)$ and having radius $R_S$, as shown in Fig. C-1. We first find the direction $\hat{\Omega}_0 = (\alpha_0,\beta_0,\gamma_0)$ from $(x,y,z)$ to $(X_S,0,0)$, which is given by

$$\alpha_0 = \frac{X_S - x}{h} \tag{C-1a}$$

$$\beta_0 = \frac{-y}{h} \tag{C-1b}$$

$$\gamma_0 = \frac{-z}{h} \; , \tag{C-1c}$$

where

$$h = [(X_S - x)^2 + y^2 + z^2]^{1/2} \; . \tag{C-2}$$

We then find the scatter angle, $\theta_0$, between $\hat{\Omega}$ and $\hat{\Omega}_0$, which is given by

$$\theta_0 = \cos^{-1}\left[\frac{\alpha(X_S - x) - \beta y - \gamma z)}{h}\right] \tag{C-3}$$

since $\cos\theta_0 = \hat{\Omega} \cdot \hat{\Omega}_0$.

The sphere projects a circle of radius $R_S$. In order to force a scatter into the solid angle of the sphere, we must pick a scatter angle, $\theta$, in the interval $(\theta_{0-},\theta_{0+})$, where

$$\theta_{0\pm} = \theta_0 \pm \theta_m \; , \tag{C-4}$$

with

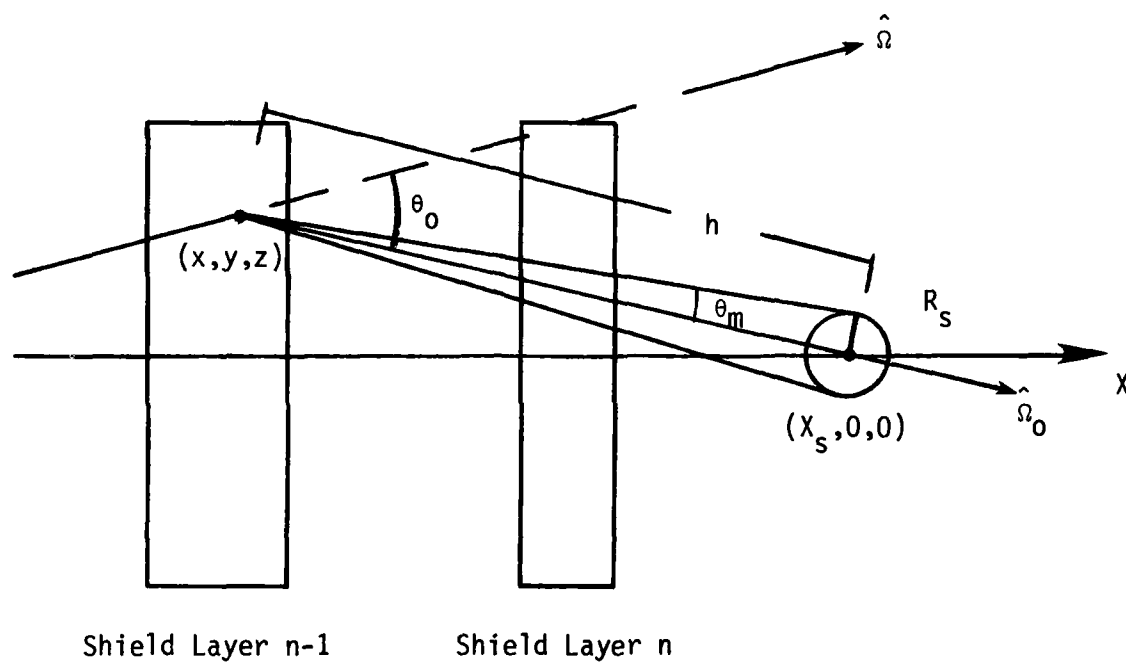$$\theta_m = \tan^{-1}\frac{R_S}{h} \; . \tag{C-5}$$

Figure C-1.  Geometry for Forcing
Scatter Toward Target Sphere

This interval defines the region between two cones that are tangent to the sphere. To force $\theta$ into this region, we pick $\cos\theta$ uniformly from that region for isotropic scattering or from the Klein-Nishina formula for Compton scattering. Thus for isotropic scattering, we pick

$$\cos\theta = \cos\theta_{0-} + \xi[\cos\theta_{0+} - \cos\theta_{0-}] \tag{C-6}$$

with weight

$$W_\theta = \frac{[\cos\theta_{0+} - \cos\theta_{0-}]}{2} \; . \tag{C-7}$$

or Compton scattering, we pick $\delta$ from $g(\delta|n)$ with

$$\delta_0 = 1 + n[1 - \cos\theta_{0-}] \tag{C-8a}$$

$$\delta_1 = 1 + n[1 - \cos\theta_{0+}] \tag{C-8b}$$

and apply the weight factor

$$W_\theta = \frac{\int_{\delta_0}^{\delta_1} g(\delta|n)dn}{D} \tag{C-9}$$

where $n$, $\delta$, $g$, and $D$ are given in Appendix A. Then we obtain $\theta$ from

$$\theta = \cos^{-1}\left[\frac{n + 1 - \delta}{n}\right] . \tag{C-10}$$

Now, given $\theta$ we need to force $\phi$ into an interval $2\Delta\phi$ wide, where

$$\Delta\phi = \tan^{-1}\left[\frac{(R_s^2 - u^2)^{1/2}}{h}\right] \tag{C-11}$$

with

$$u = h \tan(\theta_0 - \theta) \; . \tag{C-12}$$

The weight factor for forcing $\phi$ into an interval of width $2\Delta\phi$ is

$$W_\phi = \frac{\Delta\phi}{\pi} \; . \tag{C-13}$$

60

# APPENDIX D

## MCNS CODE INPUT/OUTPUT

The results reported herein were generated using a FORTRAN code called MCNS, whose logic is outlined in Chapter III. Input to the code is fairly simple; the required input format is identified in Table D-1 and the input variables are defined in Table D-2. The code uses several logical variables to specify available options. For instance, the value LISO = True causes all scattering events to be treated as isotropic and nonenergy-degrading, which is useful in code verification; the normal value LISO = False allows the code to sample post-Compton conditions from the Klein-Nishina differential scattering formula. Also, the logical variable LEVEN is used to specify whether or not the simplified geometry of Chapter II is being used. If it is, the code input requirements are simplified.

The code operates in double precision and at present is dimensioned to allow 20 shield layers, 8 energy intervals in the input spectrum, 10 annular rings for scoring the target dose and 3 elements (hydrogen, oxygen and lead). The code is reasonably efficient, due to the use of last-flight estimators, analytic equivalence and the forcing of scattered photons into the solid angle of the target sphere. Typically, 8,000 incident photon histories were used for a shield of four mean free paths thickness and 2,000 histories for shields whose total thickness was one mean free path. Sample standard deviations were typically less than 0.5 percent.

The code was written in modular form and thus can easily be extended to consider more complex situations. For instance, it would be a straightforward matter to replace the plane-parallel layers by conic or curved-surface layers, to add new elements to the cross-section library or to allow layers whose densities or compositions varied from one to another.

TABLE D-1. MCNS CODE INPUT

| Record Number | Variables | Format |
|---|---|---|
| 1 | IDATE(I), I = 1,3 | 3I10 |
| 2 | IW, IX, IY, IZ | 4I10 |
| 3 | LRITE, LRAL, LISO, LEVEN, LOUT | 5(9X,L1) |
| 4 | NHIS, NSH, NUME, NE, NRING | 5I10 |
| | If NHIS ≤ 0, Stop | |
| 5 | RSAT, TSAT, RSPH, RCEN, CUTOFF | 4F10.0 |
| | If LEVEN = True, go to record 9 | |
| 6 | SPSH(I), I = 1,2,..., NSH | 7F10.0 |
| 7 | TSH(I), I = 1,2,..., NSH | 7F10.0 |
| 8 | XSAT | F10.0 |
| | Go to 10 | |
| 9 | CAPT, CAPD, SMD | 3F10.0 |
| 10 | WTS(I,K), K = 1,2,..., NE; I = 1 | 7F10.0 |
| | Repeat record 10 for I = 1,2,..., NSH+1 | |
| 11 | RHO(I), I = 1,2,...,NSH+1 | |
| | If NUME > 0, go to record 13 | |
| 12 | ES | F10.0 |
| | Go to record 4 | |
| 13 | EC(J), J = 1,2,...,NUME+1 | 7F10.0 |
| 14 | SE(J), J = 1,2,...,NUME | 7F10.0 |
| | Go to record 4 | |

TABLE D-2. MCNS CODE INPUT VARIABLE DESCRIPTIONS

| Variable Name | Description | Units |
|---|---|---|
| IDATE(I), I=1,2,3 | Month, day, run number | |
| IW,IX,IY,IZ | Random number generator initial seeds | |
| LRITE | Logical variable; if T, detailed results are output; in F, only final results are output | |
| LRAL | Logical variable; if T, Rayleigh scattering is simulated; if F, Rayleigh scattering is neglected | |
| LISO | Logical variable; if T, scattering is isotropic and no energy is lost in a scatter; if F, scattering follows Klein-Nishina model | |
| LEVEN | Logical variable; if T, shield layering is even and simplified input option is invoked; if F, detailed input is used | |
| LOUT | Logical variable; if T, results also written to output file on logical unit 4; if F, results only written to line printer | |
| NHIS | Number of MC histories | |
| NSH | Number of shield layers | |
| NUME | Number of energy intervals in source spectrum | |
| NE | Total number of elements in all shields and the target | |
| NRING | Number of concentric rings on first shield layer for scoring contributions to dose | |
| RSAT | Radius of target cylinder | (cm) |
| TSAT | Thickness of target cylinder | (cm) |
| RSPH | Radius of target sphere | (cm) |
| RCEN | Radius of central sphere for forced target scoring | (cm) |
| CUTOFF | Cutoff value of the product of photon energy and history weight below which the photon history is terminated | (MeV) |

TABLE D-2. MCNS CODE INPUT VARIABLE DESCRIPTIONS (Continued)

| Variable Name | Description | Units |
|---|---|---|
| SPSH(I) | Spacing between shield layers I-1 and I | (cm) |
| TSH(I) | Thickness of shield layer I | (cm) |
| XSAT | X-coordinate of target left face | (cm) |
| CAPT | Total thickness of all shield layers | (cm) |
| CAPD | Distance from the front face of first shield layer to front face of target cylinder | (cm) |
| SMD | Separation between front face of target cylinder and back face of nearest shield layer | (cm) |
| WTS(I,K) | Weight fraction of element K in shield layer I > 0, or target (I = 0) | |
| RHO(I) | Density of shield layer (I ≤ NSH) or target (I = NSH+1) | $(gm/cm^3)$ |
| ES | Source energy, if monoenergetic (NAME=0) | (MeV) |
| EC(J) | Energy spectrum cutoff points such that Jth energy interval is between EC(J-1) and EC(J) | (MeV) |
| SE(J) | Fractional part of spectrum in energy interval J | |

# DISTRIBUTION LIST

DEPARTMENT OF DEFENSE

Asst to the Sec of Def, Atomic Energy
    ATTN:  Executive Assistant

Defense Communications Agency
    ATTN:  CCTC

Defense Intelligence Agency
    ATTN:  DB-40
    ATTN:  DT-1C
    ATTN:  DT-2
    ATTN:  DT-2, T. Dorr

Defense Nuclear Agency
    ATTN:  NASF
    ATTN:  SPSS
    ATTN:  SPTD
    ATTN:  STNA
    ATTN:  STSP
3 cys ATTN:  SPAS
4 cys ATTN:  STTI-CA

Defense Technical Information Center
2 cys ATTN:  DD

Field Command, DNA, Det 1
Lawrence Livermore National Lab
    ATTN:  FC-1

Field Command, DNA
    ATTN:  FCPR
    ATTN:  FCTT
    ATTN:  FCTXE
    ATTN:  FCTT, W. Summa

Joint Chiefs of Staff
    ATTN:  GD10, J-5 Nuc & Chem Div
    ATTN:  GD50, J-5 Force Plng & Prog Div
    ATTN:  SAGA/SSD
    ATTH:  SAGA/SFD

Joint Strat Tgt Planning Staff
    ATTN:  JLKS
    ATTN:  JlK, DNA Rep

Under Secy of Def for Rsch & Engrg
    ATTN:  Strat & Space Sys (OS)
    ATTN:  Engr Tech, J. Persh
    ATTN:  Strat & Theater Nuc For, B. Stephan

DEPARTMENT OF THE ARMY

BMD Advanced Technology Center
    ATTN:  ATC-T, M. Capps

Dep Ch of Staff for Ops & Plans
    ATTN:  DAMO-NCZ

Dep Ch of Staff for Rsch Dev & Acq
    ATTN:  DAMA-CSS-N

Harry Diamond Laboratories
    ATTN:  DELHD-NW-P
    ATTN:  DELHD-NW-P, J. Gwaltney
    ATTN:  DELHD-TF

DEPARTMENT OF THE ARMY (Continued)

US Army Ballistic Research Labs
    ATTN:  DRDAR-BLT, D. Menne
    ATTN:  DRDAR-BLV, W. Schuman, Jr
    ATTN:  DRDAR-BLT, J. Keefer
    ATTN:  DRDAR-BLV, R. Vitali
    ATTN:  DRDAR-BL, R. Eichelberger
    ATTN:  DRDAR-BLA-S, Tech Lib

US Army Material & Mechanics Rsch Ctr
    ATTN:  DRXMR-HH, J. Dignam

US Army Materiel Dev & Readiness Cmd
    ATTN:  DRCDE-D, L. Flynn

US Army Nuclear & Chemical Agency
    ATTN:  Library

US Army Research Office
    ATTN:  P. Radkowski, Consultant

US Army TRADOC Sys Analysis Actvy
    ATTN:  ATAA-TDC, R. Benson

USA Missile Command
    ATTN:  DRSMI-RKP, W. Thomas
    ATTN:  DRSMI-RHB, H. Greene
    ATTN:  DRSMI-RH

DEPARTMENT OF THE NAVY

Naval Research Laboratory
    ATTN:  Code 2627, Tech Lib
    ATTN:  Code 7908, A. Williams
    ATTN:  Code 4770, G. Cooperstein

Naval Sea Systems Command
    ATTN:  SEA-0352, M. Kinna

Naval Surface Weapons Center
    ATTN:  Code F31
    ATTN:  Code R15, J. Petes
    ATTN:  Code K06, C. Lyons

Naval Weapons Evaluation Facility
    ATTN:  Code 70, L. Oliver
    ATTN:  Code 70, R. Tillery

Ofc of the ceputy Chief of Naval Ops
    ATTN:  NOP 654, Strat Eval & Anal Br

Strategic Systems Project Office
    ATTN:  NSP-272
    ATTN:  NSP-273
    ATTN:  NSP-2722

DEPARTMENT OF THE AIR FORCE

Aeronautical Systems Division
    ATTN:  ASD/ENSSA, D. Sorgen
2 cys ATTN:  ASD/ENSSS, D. Ward

Air Force Geophysics Laboratory
    ATTN:  D. McLeod

65

DEPARTMENT OF THE AIR FORCE (Continued)

Air Force Rocket Propulsion Lab
    ATTN: LKLP, G. Beale

Air Force Systems Command
    ATTN: SDM
    ATTN: XRTO

Air Force Technical Applications Ctr
    ATTN: TF

Air Force Weapons Laboratory
    ATTN: NTATE, A. Sharp
    ATTN: NTES
    ATTN: SUL
    ATTN: HO, W. Minge
2 cys ATTN: NTO

Air Force Wright Aeronautical Lab
    ATTN: FIMG
    ATTN: FIBAC, D. Roselius

Air Force Wright Aeronatuical Lab
    ATTN: MLBT, G. Schmitt

Air University Library
    ATTN: AUL-LSE

Arnold Engrg Dev Center
    ATTN: AEDC, DOFOV

Ballistic Missile Office
    ATTN: EN
    ATTN: ENSN
    ATTN: ENMR
    ATTN: ENSN, W. Wilson
    ATTN: SYM
2 cys ATTN: ENSN, Blankinship

Dep Ch of Staff, Rsch, Dev & Acq
    ATTN: AFRD
    ATTN: AFRDQI

Foreign Technology Division
    ATTN: SDBS, J. Tuss
    ATTN: TQTD
    ATTN: SDBG

Electronic System Division
2 cys ATTN: ESD/OCS

Directorate of Operations
    ATTN: AFXOOTS

Strategic Air Command
    ATTN: NRI/STINFO Library
    ATTN: XPFS

DEPARTMENT OF ENERGY

Office of Military Application
    ATTN: OMA/RD&T

OTHER GOVERNMENT AGENCY

Central Intelligence Agency
    ATTN: OSWR/NED

NATO

NATO School, SHAPE
    ATTN: US Documents Officer

DEPARTMENT OF ENERGY CONTRACTORS

University of California
Lawrence Livermore National Lab
    ATTN: L-8, P. Chrzanowski
    ATTN: L-262, J. Knox
    ATTN: L-125, J. Keller

Los Alamos National Laboratory
    ATTN: R. Selden
    ATTN: D. Kerr
    ATTN: MS670, T. Scolman
    ATTN: R. Thurston
    ATTN: MS F668, R. Dingus
    ATTN: J. Hopkins

Sandia National Laboratories
    ATTN: T. Cook
    ATTN: H. Norris
    ATTN: Library & Security Classification Div

Sandia National Laboratories
    ATTN: Org 7112, A. Chabai
    ATTN: M. Cowan

DEPARTMENT OF DEFENSE CONTRACTORS

Acurex Corp
    ATTN: C. Powars
    ATTN: C. Nardo

Advanced Research & Applications Corp
    ATTN: A. Larson

Aerojet General Corp
    ATTN: R. Steele

Aerospace Corp
    ATTN: R. Crolius
    ATTN: H. Blaes

Analytic Services, Inc
    ATTN: J. Selig

APTEK, Inc
    ATTN: T. Meagher

Applied Research Associates, Inc
2 cys ATTN: W. Dunn
2 cys ATTN: F. O'Foghludha

AVCO Systems Division
    ATTN: Document Control
    ATTN: J. Stevens
    ATTN: J. Gilmore
    ATTN: W. Broding
    ATTN: W. Reinecke
    ATTN: P. Grady
    ATTN: A. Pallone

Battelle Memorial Institute
    ATTN: E. Unger
    ATTN: M. Vanderlind

BDM Corp
    ATTN: D. Shaeffer

Boeing Co
    ATTN: M/S 13-13, R. Dyrdahl

DEPARTMENT OF DEFENSE CONTRACTORS (Continued)

Boeing Co
    ATTN: W. Hammon
    ATTN: M/S 41-52, M. Susman
    ATTN: M/S 85/20, E. York
    ATTN: R. Holmes
    ATTN: M/S 41-10, J. Avery

Boeing Military Airplane Co
    ATTN: MS 75-74, D. Sawdy

California Research & Technology, Inc
    ATTN: K. Kreyenhagen
    ATTN: M. Rosenblatt

Calspan Corp
    ATTN: M. Dunn
    ATTN: M. Holden

Carpenter Research Corp
    ATTN: H. Carpenter

du Pont Chemical Corp
    ATTN: F. Bailey

G. B. Laboratory, Inc
    ATTN: G. Burghart

General Electric Co
    ATTN: B. Maguire
    ATTN: A. Garber
    ATTN: N. Dispensiere

General Research Corp
    ATTN: J. Mate

H-TECH Labs, Inc
    ATTN: B. Hartenbaum

Harold Rosenbaum Associates, Inc
    ATTN: G. Weber

Hercules, Inc
    ATTN: P. McAllister

Institute for Defense Analyses
    ATTN: Classified Library

Kaman AviDyne
    ATTN: S. Criscione
    ATTN: N. Hobbs
    ATTN: R. Ruetenik

Kaman Sciences Corp
    ATTN: J. Keith
    ATTN: F. Shelton
    ATTN: J. Harper
    ATTN: J. Hoffman

Kaman Tempo
    ATTN: B. Gambill
    ATTN: DASIAC

Kaman Tempo
    ATTN: DASIAC
    ATTN: D. Sachs

Lockheed Missiles & Space Co, Inc
    ATTN: F. Borgardt

Lockheed Missiles & Space Co, Inc
    ATTN: R. Walz

Martin Marietta Denver Aerospace
    ATTN: E. Strauss

McDonnell Douglas Corp
    ATTN: M. Potter

McDonnell Douglas Corp
    ATTN: P. Lewis, Jr
    ATTN: D. Dean
    ATTN: H. Berkowitz
    ATTN: L. Cohen, MS 13-3
    ATTN: R. Reck
    ATTN: G. Johnson
    ATTN: E. Fitzgerald

Morton Thiokol, Inc
    ATTN: J. Hinchman
    ATTN: MS 281, M. Janis

National Academy of Sciences
    ATTN: National Materials Advisory Board

Pacific-Sierra Research Corp
    ATTN: G. Lang
    ATTN: H. Brode, Chairman SAGE

Pan Am World Service, Inc
    ATTN: AEDC/Library Doc, Trf

PDA Engineering
    ATTN: J. McDonald
    ATTN: J. Dunn
    ATTN: M. Sherman
    ATTN: J. Schutzler

Physics International Co
    ATTN: J. Shea

R&D Associates
    ATTN: F. Field
    ATTN: W. Graham
    ATTN: P. Rausch
    ATTN: P. Haas

Rand Corp
    ATTN: B. Bennett

Rand Corp
    ATTN: R. Rapp
    ATTN: P. Davis

Rockwell International Corp
    ATTN: R. Hemann

Rockwell International Corp
    ATTN: G. Perroue

S-CUBED
    ATTN: G. Gurtman
    ATTN: R. Duff

Science Applications, Inc
    ATTN: W. Layson
    ATTN: J. Cockayne

Science Applications, Inc
    ATTN:  J. Warner
    ATTN:  W. Yengst
    ATTN:  W. Plows
    ATTN:  J. Manship
    ATTN:  J. Stoddard

Science Applications, Inc
    ATTN:  A. Martellucci

Southern Research Institute
    ATTN:  C. Pears

SRI International
    ATTN:  D. Curran
    ATTN:  G. Abrahamson
    ATTN:  H. Lindberg

System Planning Corp
    ATTN:  J. Luquier

Toyon Research Corp
    ATTN:  J. Cunningham
    ATTN:  B. Gragg

TRW Electronics & Defense Sector
    ATTN:  P. Brandt
    ATTN:  N. Lipner
    ATTN:  A. Zimmerman
    ATTN:  M. King
    ATTN:  D. Baer
    ATTN:  R. Plebuch
    ATTN:  W. Wood
    ATTN:  R. Bacharach
    ATTN:  M. Seizew

TRW Electronics & Defense Sector
    ATTN:  E. Allen
    ATTN:  L. Berger
    ATTN:  E. Wong
    ATTN:  V. Blankenship
    ATTN:  W. Polich
    ATTN:  D. Glenn
    ATTN:  D. Kennedy
    ATTN:  P. Dai
    ATTN:  N. Guiles

# END

## FILMED

6-85

## DTIC